A Multiscale Investigation into the Electroplastic Effects in Copper: Experiments and Crystal Plasticity Modeling

Kaiwei Wu[a,b], Xiaochuan Sun[c*], Bowen Liu[a,d], Quan Li[e], Wei Wen[f], Qiwei Shi[a*], Zhutian Xu[g], Linfa Peng[g], Huamiao Wang[h*], Yin Zhang[i], Samuel Forest[b]

a. SJTU-Paris Elite Institute of Technology, Shanghai Jiao Tong University, Shanghai, 200240, P.R. China
b. Mines Paris, PSL University, Centre des matériaux, CNRS UMR 7633, 21 Allée des Marronniers, 78000 Versailles, France
c. State Key Laboratory of Metal Matrix Composites, Shanghai Jiao Tong University, Shanghai, 200240, P.R. China
d. Mines Paris, PSL University, Centre de Mise en Forme des Matériaux (CEMEF), CNRS UMR7635, 06904 Sophia Antipolis, France
e. Max Planck Institute for Sustainable Materials, Max-Planck-Str. 1, 40237, Düsseldorf, Germany
f. School of Engineering, Lancaster University, Lancaster LA1 4YW, UK
g. State Key Laboratory of Mechanical System and Vibration, Shanghai Jiao Tong University, Shanghai 200240, P.R. China
h. Shanghai Institute of Applied Mathematics and Mechanics, School of Mechanics and Engineering Science, Shanghai University, Shanghai, 200072, P.R. China
i. Department of Mechanics, School of Mechanics and Engineering Science, Peking University, Beijing 100871, P.R. China

*Corresponding author emails: garaireen@sjtu.edu.cn (Dr. Xiaochuan Sun); sqw@sjtu.edu.cn (Dr. Qiwei Shi); wanghm@shu.edu.cn (Dr. Huamiao Wang)

Abstract

Electroplastic effects in metals show measurable changes of exerted force in deformation processes under certain electric current conditions, holding potential to facilitate metal forming. However, the application of these effects is hindered by the so far unclear image of the underlying mechanisms, and the corresponding contributions are debatable. This work aims to quantitatively elucidate the athermal mechanisms of electroplasticity in copper with experimental and computational methods combined. Temperature-controlled pulsed-current electricity-assisted deformation (EAD) tests were conducted to emphasize athermal contributions, while large-area EBSD, two-beam TEM, and high-resolution EBSD (HR-EBSD) measurements were used to characterize texture evolution, slip systems, and semi-quantitative dislocation density. Then, a crystal plasticity model, incorporating electroplasticity-related mechanisms with thermodynamic evolution formulas, was applied to support a mechanism-focused interpretation of the observed electroplastic responses from dislocation behaviors. Analysis reveals that the reduced work hardening observed in the stress-strain curves originates from fluctuations in the local response. These fluctuations exhibit a characteristic two-stage behavior, consisting of an “rapid drop” followed by a “slow decline” of stress response. The associated changes in maximum flow stress and macroscopic work-hardening rate arise from the cumulative effect of EAD-induced softening during current pulses, which is linked to the recovery of statistically stored dislocations (SSDs). By quantitatively connecting short-term information to macroscopic stress-strain evolution within an

electricity-coupled crystal plasticity framework and comparing with experimental textures and dislocation densities, this work provides mechanistic interpretations of athermal mechanisms and consolidate the understanding of electroplasticity in metals.

Keywords: Electroplasticity, Electricity-assisted deformation, Athermal effect, Electricity-coupled crystal plasticity, Dislocation recovery.

1. Introduction

Electroplastic effects during electricity-assisted deformation (EAD) have long been recognized for their potential to tailor mechanical properties (Ruszkiewicz et al., 2017). By applying alternating (AC) or direct current (DC) during metal forming, flow stress reductions (He et al., 2020; Ruszkiewicz et al., 2017; Xu et al., 2022; Zhang et al., 2018), changes in the maximum elongation (He et al., 2020; Li et al., 2022a; Xu et al., 2022; Zhang et al., 2018; Zhao et al., 2021), and variations in work-hardening rate (Kim et al., 2017; Xu et al., 2022; Zhao et al., 2021) have been reported. These effects have practical applications for processes such as thin-wall structure forming and forging (Jones and Mears, 2011; Jones et al., 2012; Li et al., 2022a; Siopis et al., 2011). Therefore, understanding the underlying physics of electroplastic effects is crucial for designing and optimizing EAD-assisted manufacturing processes.

Electroplasticity during EAD is driven by multiple mechanisms, including Joule heating and athermal effects arising from electron-dislocation interactions or other electric-field-induced processes. While Joule heating has been widely invoked to explain stress drops in metals such as steels (Tang et al., 2000), titanium alloys (Dimitrov et al., 2021; Kinsey et al., 2013; Lee et al., 2017) and copper (He et al., 2020)(Xu et al., 2022; Zhang et al., 2018), however, recent studies demonstrate that electric current can also directly modify dislocation activity, enhance ductility, or alter flow stress independent of measurable temperature rise (Chuan et al., 2024; Niu et al., 2025; Zhao et al., 2021). Decoupling these effects is usually challenging, as thermal, electromagnetic, and stress field are coupled together. Endeavors have been made to decouple these effects.

On theoretical side, researchers proposed diverse propositions. The electron wind force, acting proportionally to the value of current density, exert additional driving force on dislocation motion (Ren and Wang, 2025; Xu et al., 2023) . Others proposed electron-dislocation scattering (Dai et al., 2024; Li et al., 2013; Xu et al., 2023) as mechanism, which is proposed as energy transfer to dislocation core area and thus lower the corresponding energy barrier for dislocation evolution. In addition, the magnetoplastic effect exist in metals and suggest that current-induced magnetic fields can also enhance dislocation mobility (Aksenova et al., 2022; Alshits et al., 1997; Molotskii and Fleurov, 1997a, b; Molotskii, 2000). On experimental side, experiments on incoherent twining boundaris (ITBs) (Li et al., 2022c) and mechanical tests on e-beam irradiated Au foils (Stangebye et al., 2022) suggested electron-dislocation scattering as the key mechanism, while electricity-coupled Ni single-crystal (Li et al., 2022b) and Ni alloy (Zhang et al., 2020) tests are in favour of the electron-wind force. Under electro-magnetic field, experimental studies have also proposed significant magnetoplastic effects existing in metals (Aksenova et al., 2022; Guo et al., 2022; Jemielniak and Krolikowski, 1985; Yang et al., 2023b). In general, a multitude of potential electroplastic mechanisms exist, each exerting distinct influences on dislocation dynamics and contributing to varying degrees to the specific mechanical response.

The complexity of the mechanisms makes the discussions conflict in published reports. Taking copper as an example, pure copper shows significant flow stress reduction (Fig. 1(b-c)) and texture evolution under some conditions (Fig. 1(d)), while other studies report negligible or opposite trends (Fig. 1(a, e)) (Chuan et al., 2024; Dimitrov et al., 2021; Lee et al., 2017; Niu et al., 2025; Zhang et al., 2018). Subtle stress-strain fluctuations are often overlooked due to low temporal resolution, which contains information on electroplastic mechanisms. These inconsistencies emphasize the need for controlled experiments to decouple thermal and athermal effects. Copper, with high electrical and thermal conductivity (Lu et al., 2004), is an ideal model. Careful pulsed-current design and cooling keep temperature rise minimal (~few K) (He et al., 2020; Rudolf et al., 2021; Zhang et al., 2018), ensuring observed responses primarily reflect athermal mechanisms and justifying the experimental design in this study.

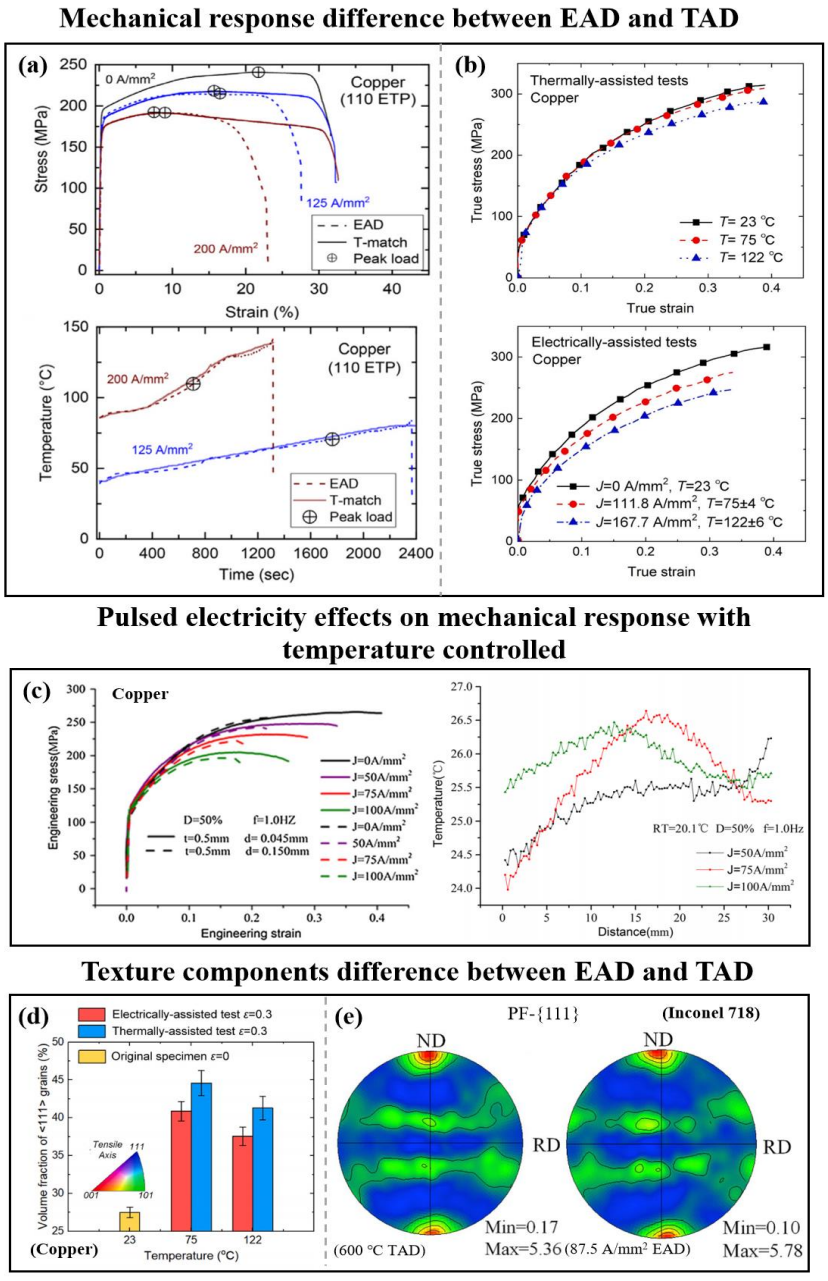

Fig. 1 Reports on electroplasticity in copper (a-d) and Inconel 718 (e). (a-b) Stress response differences

between electricity-aided deformation (EAD) under various current intensities and profiles and thermally-assisted deformation (TAD) tests with matched temperature (Rudolf et al., 2021; Xu et al., 2022) (c) Mechanical behavior during pulsed EAD with temperature controlled (Zhang et al., 2018) (d) Comparative analysis of <111> component intensity in deformed textures corresponding to processes depicted in (b) (Xu et al., 2022). (e) Pole figures illustrating deformed textures under EAD and TAD with equivalent temperature conditions (Liu et al., 2022).

Numerical modeling is indispensable for uncovering electroplastic mechanisms, as completely in-situ characterization is usually difficult under varying electromagnetic fields present in the samples. Discrete dislocation dynamics (DDD) simulations capture microscale mechanisms (Xu et al., 2023) but lack direct multiscale validation. Crystal plasticity finite element methods (CPFEM) have been effective for small deformations (~2% strain) (Lahiri et al., 2019; Yang et al., 2023a), yet their application to industrial-scale pulsed-current electrically assisted deformation (EAD) faces significant computational challenges (Xu et al., 2022) due to the need for extremely small time increments and repeated integration within each current pulse. As a result, most large-strain CPFEM studies are restricted to one or two pulses or assume steady current conditions (Gao et al., 2022; Tiwari et al., 2022; Zheng and Yi, 2025). Macroscopic models, such as modified Kocks-Mecking formulations (Dai et al., 2024; Niu et al., 2025) capture overall stress responses but cannot resolve texture evolution or quantitative dislocation density changes. To bridge this gap, the dislocation density-based elastic visco-plastic self-consistent (EVPSC) framework offers an effective compromise, enabling simultaneous prediction of mechanical response, dislocation evolution, and texture development with manageable computational cost (Lebensohn and Tomé, 1993; Wang et al., 2017; Wang et al., 2010; Zhu et al., 2021). In the present work, combining pulsed EAD experiments results with an electricity-coupled EVPSC model provides a mechanism-oriented study for interpreting large-strain electroplastic deformation.

In this study, we investigate the athermal mechanisms of electroplasticity in copper using a combined strategy that integrates temperature-controlled pulsed EAD experiments with an electricity-coupled, dislocation-based crystal plasticity model. Experiments serve to constrain and validate the constitutive model description, enabling quantitative assessment of dislocation-level mechanisms at different deformation stages. This integrated approach provides a unified physical interpretation of electroplastic responses and reconciles previously debated observations in the literature.

For clarity, the organization of this paper is as follows. Section 2 describes the experimental setup and loading parameters for the EAD tests, together with the basic material characterization procedures. Section 3 presents the theoretical framework of the electricity-coupled crystal plasticity model. In Section 4, we first provide analysis of the mechanical responses and microstructural characterization results, then calibrate the crystal plasticity model against experiments and validate it. Finally use the multiscale information obtained from the model to further elucidate the deformation mechanisms governing EAD.

2. Materials and experiment results

2.1. Material and sample preparation

The samples used in this study were fabricated from rolled industrially pure copper sheets with a nominal composition of 99.9% Cu. All specimens were sectioned from the same sheet to ensure consistency in material provenance. The detailed configuration of the cut samples is demonstrated in Fig.

2, showing a “two-ear” dog-bone shaped characteristic with a thickness of 1mm. All cut copper specimens were annealed at 450 °C for 1 hour.

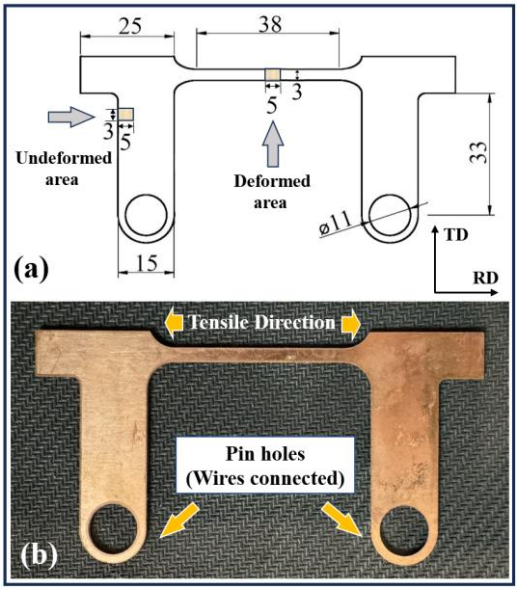

Fig. 2 (a) Geometric graph and (b) photo of the electricity-aided tensile test sample with pin holes connected to the electricity wires. EBSD samples are chosen from the undeformed area and the deformed area shown in (a). Tension tests were performed along RD.

2.2. Tensile test setup

Mechanical experiments were carried out on a custom-designed platform (Fig. 3) built on a standard ZwickRoell tensile machine, equipped with phenolic-resininsulated collets to prevent electrical damage under high current. To investigate the athermal effect of electricity, specimen temperature was strictly controlled: a chilled-air cooling unit was continuously operated about 15 cm from the sample, while surface temperature was monitored in real time with a laser-calibrated infrared thermometer (TASI Electronics Co., Ltd.) to capture temperature fluctuations. The measure resolution of machine has been analyzed to be ±0.035 MPa (see in Appendix 4).

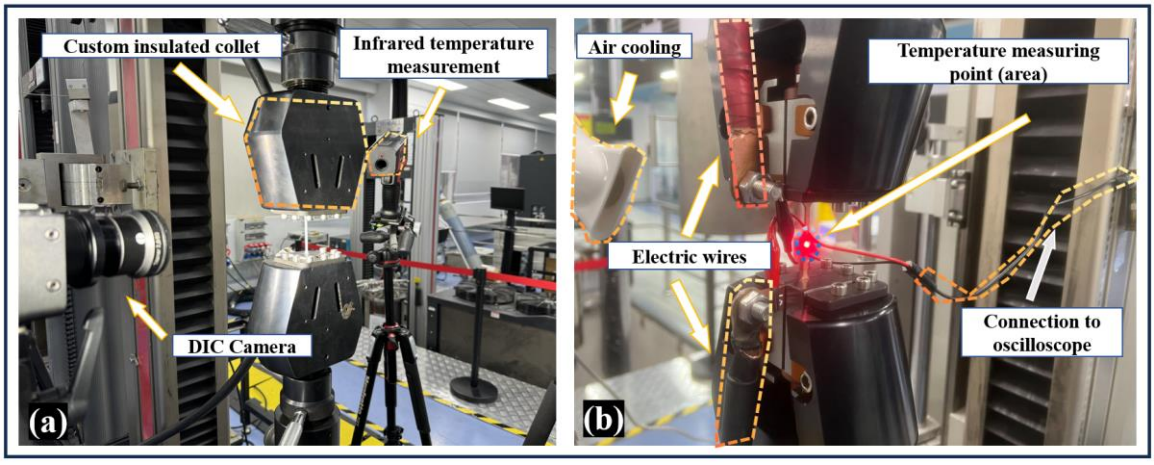

Fig. 3 Experimental setup for electricity-assisted tensile testing, featuring a custom insulated collet,

infrared temperature measurement, chilled-air cooling, and an oscilloscope connected to the sample.

Current densities of 100 A/mm² and 133 A/mm² were applied at 2.5 Hz with a 20% duty time, chosen to minimize heating and enable reproducible simulations. The temporal current waveforms (Fig. 4) exhibit capacitive charging behavior, well fitted by a classical exponential function (as presented in Eq. (1)) (Fig. 4) and subsequently used in simulations.

$$J(t) = J_{max}\left[1 - \exp\left(\frac{-(t+\Delta t)}{\tau_t}\right)\right], \qquad nT < t < (n+0.2)T \tag{1}$$

where J_{max} refers to the applied current density and τ_t refers to the characteristic time of a charging process and Δt is the temporal phase difference. During tensile tests, all samples were deformed at a constant engineering strain rate of 5×10^{-3} s^{-1}, with a maximum engineering strain of 0.3, prior to the fracture strain (~ 0.4) of similar samples (Xu et al., 2022). Each tensile test contains 150 cycles of pulses with a duration of 60 seconds. All EAD tests were conducted with real-time compliance correction and a control frequency of 1000 Hz (control cycle ≈ 1 ms), sufficient to maintain constant strain rate during the electricity working time (80 ms). The sample temperatures were controlled close to ambient (~296 K) throughout all tensile tests. The detailed demonstration of the temperature evolution is provided in the Supplementary Materials.

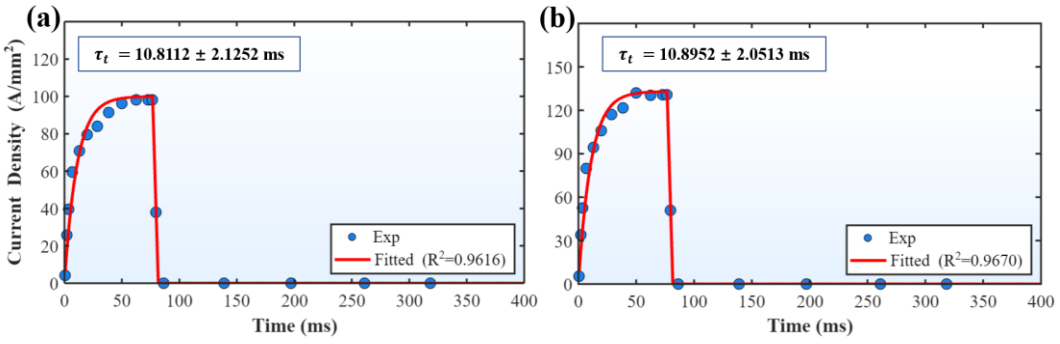

Fig. 4 (a-b) Charging current waveform at 100 A/mm² and 133 A/mm², 20% duty ratio.

2.3. Microstructure measurements

After the electro-mechanical coupling experiments, the microstructure was characterized using electron backscatter diffraction (EBSD) and transmission electron microscopy (TEM). EBSD analysis was performed on undeformed and deformed regions (Fig. 2a) using a system from EDAX Inc. (USA). Specimens were electro-polished in a phosphoric acid–ethanol solution (1:9 by volume) at −20 °C under 28 V and 0.9 A for 30 s. Scans were conducted over a 1000 μm × 1000 μm area with a 1 μm step size to obtain statistically significant information on textures and grain sizes. Kernel average misorientation (KAM) was analyzed to assess geometrically necessary dislocations (GNDs) with and without electrical current. TEM specimens were prepared by ion milling. Disc-shaped samples (3 mm diameter) were sectioned via wire EDM, mechanically ground to ~25 μm, mounted on copper grids, and thinned using a Gatan Model 691 ion milling system. Final perforation was conducted at 4 kV, followed by polishing at 3 kV for 30 min. TEM observations were performed using an FEI Talos F200X G2 microscope (FEI, USA).

Dislocation density evolution was further investigated using high-resolution EBSD (HR-EBSD), following a Williamson-Hall-plot method (Borbély, 2022) (see details in SM Part 1). HR-EBSD was

conducted on undeformed and deformed regions subjected to 100 A/mm² current, covering 200 μm × 200 μm areas with ~40,000 Kikuchi patterns collected at 1 μm step size and 128 × 156 pixels resolution. Diffraction peak widths from experimental patterns were compared with simulations to estimate relative dislocation densities. Experiments utilized an Oxford Instruments C-Swift EBSD camera, allowing quantification of GNDs (ρ_{GND}) and total dislocation density (ρ_{tot}). The ρ_{tot} increment provides a key reference for validating the EC-EVPSC model, as discussed in Section 4.3.

3. Self-consistent polycrystal model coupled with electricity

3.1. Brief description of the self-consistent polycrystalline framework

Crystal plasticity simulation is employed in this study to investigate the polycrystalline deformation history during EAD. This approach facilitates an interpretation of the electroplastic origin based on multiscale mechanisms, including the evolution of dislocation density, dislocation movement, and texture. Consequently, this research incorporates electroplastic effects into the well-established EVPSC framework (Beyerlein and Tomé, 2008; Sun et al., 2024; Wang et al., 2010a; Wang et al., 2010b; Zhu et al., 2021) and create the electricity-coupled elastic-viscoplastic self-consistent (EC-EVPSC) polycrystal model to capture electroplastic behavior. The present model incorporates electro-mechanical coupling effects of defects, accounting for key mechanisms such as reduced barriers for dislocation slip, reduced dislocation multiplication, and accelerated dislocation density recovery (Fig. 5). The EVPSC/VPSC-based framework (Lebensohn and Tomé, 1993) describes polycrystal-grain interactions via the Eshelby tensor, bridging single-crystal slip mechanisms and macroscopic behavior. This multiscale approach effectively predicts polycrystal responses under combined elastic-viscoplastic deformations. Detailed implementation procedures are provided in Refs. (Tomé and Lebensohn, 2023; Wang et al., 2010a). A brief description of the polycrystal level self-consistent mathematical scheme is present in Appendix 1.

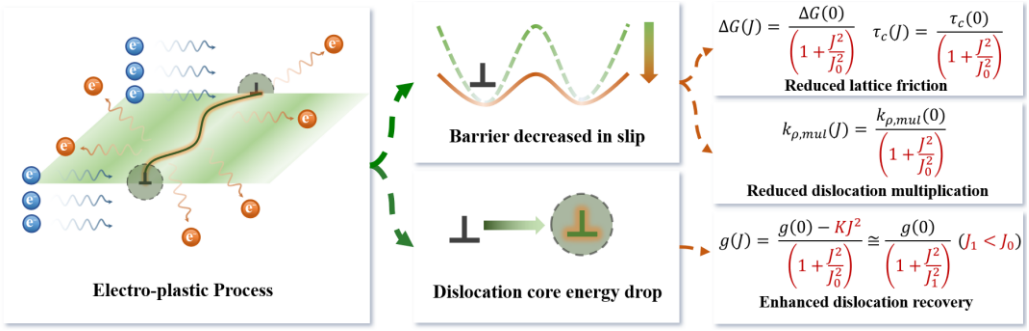

Fig. 5 Schematic representation of the athermal effects associated with electroplasticity.

3.2. The dislocation movements law and influences by electricity

In this work, the plastic deformation in each grain is the sum of dislocation-induced plasticity, calculated by summing shear strain rate tensors across multiple slip systems, where the shear strain rate in each slip system follows Orowan's equation (Orowan, 1940):

$$l_{ij}^{dis} = \sum_{\alpha=1}^{n} s_i^{\alpha} n_j^{\alpha} \dot{\gamma}^{\alpha} = \sum_{\alpha=1}^{n} s_i^{\alpha} n_j^{\alpha} \rho^{\alpha} b^{\alpha} v^{\alpha} \tag{2}$$

Here, s^{α} and n^{α} represent the slip direction and normal vector of the slip plane, respectively. $\dot{\gamma}^{\alpha}$ denotes the shear strain rate. ρ^{α}, b^{α} and v^{α} represent the dislocation density, Burgers vector

magnitude, and dislocation velocity, respectively. The slip systems considered are the conventional octahedral one in FCC metal. The Burgers vector is taken as 0.256 nm for copper (Cheong et al., 2005). The superscript α means the slip system α, similarly hereafter. The dislocation velocity is governed by the thermodynamic activation process under quasi-static loading conditions (Beyerlein and Tomé, 2008; Kocks et al., 1975; Sun et al., 2024):

$$v^{\alpha} = v_0^{\alpha} \exp\left(\frac{-\Delta G^{\alpha}}{k_B T}\right) \tag{3}$$

where the ΔG^{α} denotes the free enthalpy of activation, k_B is the Boltzmann constant, and T is the absolute temperature in Kelvin. This free enthalpy will be affected when electricity is induced to the deformation process, and this effect is going to be discussed as follows in this section.

The activation free enthalpy, as a function, depends on the resolved shear stress on slip system α, calculated as $\tau^{\alpha} = s_i^{\alpha} n_j^{\alpha} \sigma_{ij}^{g}$ where σ_{ij}^{g} is the Cauchy stress tensor in the grain coordinate system. This enthalpy can be expressed via a Taylor expansion at 0 MPa as (Beyerlein and Tomé, 2008)

$$\Delta G^{\alpha}(\tau^{\alpha}) \cong \Delta G^{\alpha}(0) + \frac{\partial \Delta G^{\alpha}(\tau^{\alpha})}{\partial \tau^{\alpha}} \tau^{\alpha} \tag{4a}$$

The $\frac{\partial \Delta G^{\alpha}(\tau^{\alpha})}{\partial \tau^{\alpha}} = -\Delta V^{\alpha *}$ denotes the activation volume (Beyerlein and Tomé, 2008; Lahiri et al., 2019; Saada, 1995). In this work this formulation is modified to include the dislocation interaction, aligned with the expression typically employed in thermodynamic activation models (Beyerlein and Tomé, 2008; Kocks et al., 1975; Wang et al., 2013):

$$\Delta G^{\alpha}\left(\tau_{eff}^{\alpha}\right) = \Delta G_0^{\alpha} - \tau_{eff}^{\alpha} \Delta V^{\alpha *} \tag{4b}$$

Here ΔG_0^{α} refers to the referenced Gibbs free energy and the τ_{eff}^{α} refers to the effective resolved shear stress, defined as $\tau_{eff}^{\alpha} = \tau^{\alpha} - \tau_f^{\alpha}$. τ_f^{α} is the friction resistance (Sun et al., 2024), primarily provided by dislocation interactions in this work (Section 3.4).

Equivalent to previous equations, the form adapted in previous works (Beyerlein and Tomé, 2008; Kocks et al., 1975) shows:

$$\Delta G^{\alpha}\left(\tau_{eff}^{\alpha}\right) = \Delta G_0^{\alpha}\left(1 - \frac{\tau_{eff}^{\alpha}}{\tau_c^{\alpha}}\right) \tag{4c}$$

where τ_c^{α} reflects the inherent strength of the slip system. In (Beyerlein and Tomé, 2008), it has been provided a form of ΔG_0^{α} and $\Delta V^{\alpha *}$ as follows:

$$\Delta G_0^{\alpha} = \frac{D^{\alpha}}{\tau_{sat}^{\alpha}} g^{\alpha} \mu b^{\alpha 3} \tag{5a}$$

$$\Delta V^{\alpha *} = \frac{D^{\alpha}}{\tau_{sat}^{\alpha}} b^{\alpha 3} \tag{5b}$$

where D^{α} is a proportionality factor dimensionally consistent with stress, interpreted as drag stress during the dislocation movement process (Beyerlein and Tomé, 2008; Sun et al., 2024; Wang et al., 2017). g^{α} and μ are respectively a normalized activation energy and the macroscopic shear modulus, and τ_{sat}^{α}

is the saturated resolved shear stress. By integrating Eq. (5) into Eq. $(4b)$ and compared with the form Eq. $(4c)$, it appears that the following relation holds:

$$\tau_c^\alpha = \mu g^\alpha \tag{6}$$

In certain prior works (Dai et al., 2024; Gao et al., 2022; Lahiri et al., 2019; Tiwari et al., 2022; Yang et al., 2023a), the effect of electric current on physical parameters has been incorporated as state variables. A similar approach is appropriate for our case, as will be illustrated through a brief magnitude estimation in the Supplementary Materials Part 3. Based on prior work, τ_c^α, which characterizes a part of the short-range barrier, is known to decrease under electric current. In this model, we adopt an analogous formulation (Lahiri et al., 2019; Yang et al., 2023a; Zheng and Yi, 2025) to capture this electromagnetic-induced softening effect.

$$\tau_c^\alpha(J) = \frac{\tau_c^\alpha}{(1+\frac{J^2}{J_0^2})} \tag{7}$$

where J is the applied current density and J_0 is the reference current density to be fitted depending on the materials used. Since previous studies on copper have reported no observable change in the elastic modulus during the elastic deformation stage (Xu et al., 2022; Zhang et al., 2018), the influence of current density on μ is considered negligible. So, the expressions for g^α and ΔG_0^α can be derived:

$$g^\alpha(J) = \frac{g^\alpha}{(1+\frac{J^2}{J_0^2})} \tag{8a}$$

$$\Delta G_0^\alpha(J) = \frac{\Delta G_0^\alpha}{(1+\frac{J^2}{J_0^2})} \tag{8b}$$

The essence of this change lies in the electromagnetic field during EAD, which results in electron spin states change (Molotskii and Fleurov, 1997b) at dislocation core and alters the effective depinning energy (Lahiri et al., 2019; Molotskii and Fleurov, 1997a, b; Molotskii et al., 1995; Yang et al., 2023a). The reduction of the depinning barrier upon the electromagnetic field has been confirmed by experiments in broad temperature range (Jemielniak and Krolikowski, 1985; Molotskii and Fleurov, 1997a; Molotskii, 2000; Molotskii et al., 1995). Thus, the dislocation motions are tended to be facilitated by the electromagnetic field during EAD. However, for non-continuous pulsed DC, the surrounding magnetic field resembles that of an AC excitation due to its time-varying nature. Under such conditions, the skin effect proved to be negligible. The skin depth is calculated as (Hayt Jr, 1989):

$$\delta_m = \sqrt{\frac{2\rho_e}{2\pi f \mu_{copper}}} \tag{9}$$

where ρ_e is the electrical resistivity (Lu et al., 2004) ($1.68 \times 10^{-8}\Omega \cdot m$), f is the frequency of current in this study (2.5Hz) and μ_{copper} is the magnetic permeability of copper ($1.26 \times 10^{-6}\mathrm{H} \cdot m^{-1}$). The numerical calculation yields a skin depth of 41.26 mm, significantly greater than half of the sample thickness (0.5 mm). In this scenario, the homogenization method is applicable and the skin effect is

ignored in this study.

3.3. The dislocation evolution mechanisms influenced by electricity

In this section, the superscript $\boldsymbol{\alpha}$ is omitted from all equations and expressions in this subsection where applicable. The influence of electric current on dislocation evolution is discussed here. For clarity and coherence, the analysis is limited to a single slip system. The dislocation evolution is considered by a modified Kocks-Mecking relationship. The evolution of dislocations in the proposed model is governed by mechanisms including multiplication and dynamic recovery (Austin and McDowell, 2011; Beyerlein and Tomé, 2008; Bong et al., 2019). The influence of electricity is incorporated inside by considering the current density as a state variable for several physical parameters. The dislocation density evolution law is expressed as (Sun et al., 2024):

$$\frac{d\rho}{d\gamma} = \frac{d\rho_{mul}}{d\gamma} - \frac{d\rho_{ann}}{d\gamma} \tag{10a}$$

$$\frac{d\rho_{mul}}{d\gamma} = \frac{k_{\rho,mul}}{\bar{L}} \tag{10b}$$

$$\frac{d\rho_{ann}}{d\gamma} = \left(\frac{d\rho_{mul}}{d\gamma}\right)\left[\frac{c_h b}{g}\left(1 - \frac{kT}{Db^3}\log\frac{|\dot{\varepsilon}|}{\dot{\varepsilon}_0}\right)\right]^2 \rho \tag{10c}$$

In this form, $k_{\rho,mul}$ controls the multiplication rate of the dislocation, $\bar{L} = 1/\sqrt{\sum_\alpha \rho_\alpha}$ represents the length of the mean free path of dislocation movements depending on the total dislocation density ($\rho_{tot} = \sum_\alpha \rho_\alpha$) (Beyerlein and Tomé, 2008; Stricker and Weygand, 2015; Sun et al., 2024; Zecevic et al., 2018) and c_h is a coefficient controlling the dislocation hardening (Sun et al., 2024). $|\dot{\varepsilon}|$ and $\dot{\varepsilon}_0$ are equivalent strain rate and the reference strain rate, respectively. Combining the three equations above yields the following result:

$$\frac{d\rho}{d\gamma} = \frac{k_{\rho,mul}}{\bar{L}} - \left(\frac{k_{\rho,mul}}{\bar{L}}\right)\left[\frac{c_h b}{g}\left(1 - \frac{kT}{Db^3}\log\frac{|\dot{\varepsilon}|}{\dot{\varepsilon}_0}\right)\right]^2 \rho \tag{10d}$$

Here, g essentially acts as a constant governing dislocation recovery. Letting Eq. (10d) to zero, the saturation dislocation density in this relation is determined by g. A smaller value of g implies a lower energy requirement for dislocation recovery, thereby resulting in a reduced saturation dislocation density.

Prior research suggests that the mean free path of dislocations in copper can be altered through the electromagnetism induction process, as presented by post-experiment measurements and simulation works (Alshits et al., 1997; Molotskii et al., 1995; Xu et al., 2022; Yang et al., 2023a). The change of the mean free path in copper with and without an electric current could be described by the following quadratic relationship:

$$\bar{L}(J) = \bar{L}(0)\left(1 + \frac{J^2}{J_0^2}\right) \tag{11a}$$

where J_0 is the same reference current density as in the previous section. In several models (Molotskii et al., 1995; Xu et al., 2022; Yang et al., 2023a), $\bar{L}$ is treated as a state constant. However, in reality, $\bar{L}$ evolves with dislocation evolution (Beyerlein and Tomé, 2008; Sun et al., 2024; Zecevic et al., 2018). In this study, we propose that the influence of electric current on $\bar{L}$ essentially arises from the effect of electromagnetic field energy on the dislocation dynamic processes. The larger $\bar{L}$ implies lower final dislocation density and decreased multiplication process. In this study, this is presented as a decrease in

the dislocation multiplication rate, which can be expressed in the following form:

$$\left.\frac{d\rho_{mul}}{d\gamma}\right|_{(J)} = \frac{\left.\frac{d\rho_{mul}}{d\gamma}\right|_{J=0}}{(1+\frac{J^2}{J_0^2})} \tag{11b}$$

which is:

$$\left.\left(\frac{k_{\rho,mul}}{\bar{L}}\right)\right|_{(J)} = \frac{k_{\rho,mul}}{\bar{L}(1+\frac{J^2}{J_0^2})} \tag{11c}$$

For more convenient implementation in simulations, the following form is adopted in this study:

$$k_{\rho,mul}(J) = \frac{k_{\rho,mul}}{(1+\frac{J^2}{J_0^2})} \tag{11d}$$

Eq. (11d) implies that the presence of electric current reduces the probability of new dislocation generation through dislocation multiplication during dislocation dynamic evolution.

Furthermore, the electric current-induced reduction in dislocation core energy decreases the annihilation barrier by introducing electrostatic forces (Sutton and Todorov, 2021) and energy transfer (Xu et al., 2023) into the dislocation core region. The dynamic dislocation recovery tends to be facilitated during plastic deformation (Ao et al., 2018; Dai et al., 2024; Tiwari et al., 2022; Xiang and Zhang, 2019; Xu et al., 2023; Zhao et al., 2019). In this work, a recently adopted quadratic decay form is used to describe the energy attenuation associated with electric current. This choice is directly supported by the De Broglie theory and has been applied in previous studies (Dai et al., 2024; Li et al., 2013; Xu et al., 2023). The linear decay form derived from classical transport theory has been shown in earlier works to be insufficient in magnitude ($\lesssim 10^{-2}$ MPa) (Li et al., 2022b; Sprecher et al., 1986) to account for the observed electroplastic effects, and is therefore not considered in the present model. Taking into account the effects already considered in Section 3.2, the expression for $g(J)$ under the combined influence of electromagnetic conditions is given as Eq. (12a):

$$g(J) = \frac{g-\Delta e}{\left(1+\frac{J^2}{J_0^2}\right)} = \frac{g-KJ^2}{\left(1+\frac{J^2}{J_0^2}\right)} = \frac{g\times\left(1-\frac{J^2}{\frac{g}{K}}\right)}{\left(1+\frac{J^2}{J_0^2}\right)} \tag{12a}$$

The term $\Delta e = KJ^2$ is a normalized statistical energy transfer due to electron-dislocation scattering (Dai et al., 2024; Li et al., 2013; Xu et al., 2023) and $\sqrt{g/K}$ has the dimension of current density. However, since $g(J)$ is a dimensionless parameter representing a statistical energy barrier and a factor of ΔG_0^{α}, we impose two assumptions: (1) $g(J) \geq 0$ at ambient temperature for all $J > 0$, consistent with its interpretation as energy barrier; (2) $\lim_{J\to+\infty} g(J) = 0$, that the barrier vanishes to zero at extremely high current densities. Thus, this modification on $g(J)$ not only regularizes the function mathematically but also preserves its physical interpretation. So, to prevent unphysical values, the following form is adopted $(12b)$:

$$g(J) \cong \frac{g \times \left(1+\frac{J^2}{\frac{g}{K}}\right)^{-1}}{\left(1+\frac{J^2}{J_0^2}\right)}$$

$$= g \times \left[1+\frac{J^2}{J_0^2}+\left(\frac{J^2}{\frac{g}{K}}\right)+\left(\frac{J^2}{J_0^2}\right)\cdot\left(\frac{J^2}{\frac{g}{K}}\right)\right]^{-1}$$

$$= g \times \left[1+\frac{J^2}{J_1^2}+\left(\frac{J^2}{J_0^2}\cdot\frac{J^2}{\frac{g}{K}}\right)\right]^{-1} \quad (12b)$$

This form captures the energy attenuation behavior proposed by (Gao et al., 2022) at large current densities, but the Gao model diverges near $J = 0$. Conversely, the classical quadratic decay associated with electron scattering approximates the behavior near $J = 0$, but diverges to negative values at very high currents. Both of these limits are physically unreasonable. In contrast, the present form satisfies the required properties at both $J = 0$ and $J \to +\infty$, maintains monotonic decay, and ensures that $g(J)$ remains non-negative, thereby preserving both mathematical consistency and physical plausibility. The descriptions in detail on this modelling are presented in Supplementary Materials Part 6.

In Eq. $(12b)$, $J_1 = \sqrt{\frac{g}{K}\cdot J_0^2/\left(J_0^2+\frac{g}{K}\right)} < J_0$ is a reduced parameter to be fitted with the dimension of the current density. Notably, the parameter J_0 has been experimentally measured and fitted in previous studies (Dai et al., 2024; Li et al., 2013) to be on the order of $\sim 10^3$ A/mm^2, and a similar magnitude will be observed in the present work. Under this magnitude, J^2/J_0^2 is estimated to be $\sim 10^{-2}$ in this study, thus the second-order term in Eq. $(12b)$ is ignored in front of $J^2/\left(\frac{g}{K}\right)$ and the equation could be simplified as:

$$g(J) \cong g \times \frac{1}{\left(1+\frac{J^2}{J_1^2}\right)}, \quad \text{with } (J_1 < J_0) \quad (12c)$$

The form of Eq. $(12c)$ is a simplified form to be considered in simulations and J_1 is the only electric-related parameter to be fitted, thus reducing the complexity of the model. This simplification is based on the real current density in this study, also applicable to other (Xu et al., 2022; Zhang et al., 2018) EAD scenarios with similar current density. This formulation closely resembles the mathematical form presented in Section 3.2, thereby facilitating more convenient mathematical processing. Finally, the dislocation density evolution law is presented as:

$$\frac{d\rho}{d\gamma} = \frac{k_{\rho,mul}}{\bar{L}\cdot\left(1+\frac{J^2}{J_0^2}\right)} - \left(\frac{k_{\rho,mul}}{\bar{L}\cdot\left(1+\frac{J^2}{J_0^2}\right)}\right)\left[\frac{c_h b}{g}\left(1+\frac{J^2}{J_1^2}\right)\left(1-\frac{kT}{Db^3}\log\frac{|\dot{\varepsilon}|}{\dot{\varepsilon_0}}\right)\right]^2 \rho \quad (13)$$

This modified constitutive law incorporates the influence of electric current during EAD tests by introducing electric current-dependent terms into the dislocation evolution framework. As a result, it effectively captures the profile of work-hardening behavior induced by EAD, allowing also for accurate simulations of local strain–stress responses, verifying the validity of Eq. (13) (in Section 4.2).

3.4. The dislocation interaction and the grain boundary effect

The electricity-induced dislocation activities will lead to a change in the slip resistance, thereby influencing the overall mechanical behaviors of polycrystalline materials. This dislocation hardening rule is based on line tension theory (Kocks, 1966) and dislocation interaction principle (Bassani and Wu, 1991; Wu et al., 1991), expressed as:

$$\tau_b = c_h \mu b \sqrt{\sum_{\beta}^{N} h^{\alpha\beta} \rho_\beta} \tag{14}$$

where $h^{\alpha\beta}$ is the latent hardening coefficient matrix, capturing the contributions of different dislocation interaction modes across slip systems (Bassani and Wu, 1991; Cuitino and Ortiz, 1993; Franciosi et al., 1980) and c_h is the Taylor relation parameter to be fitted (Sun et al., 2024; Taylor, 1934), same as the one in Eq. (15). For the twelve <110> {111} slip systems in FCC system, five interaction modes between slip systems are defined as no junction (NJ), Hirth lock (HL), coplanar junction (CJ), glissile junction (GJ), and sessile junction (SJ), determined by the Frank rule, the directional alignment of Burgers vectors, and their coplanarity. The values of the corresponding latent hardening coefficients, denoted as h_{NJ}, h_{HL}, h_{CJ}, h_{GJ} and h_{SJ}, follow the following monotone order.

$$h_{NJ} < h_{HL} < h_{CJ} < h_{GJ} < h_{SJ} \tag{15}$$

and the coefficient for the self-interaction, $h_{NJ} = h^{\alpha\alpha}$, set to 1. Previous studies (Akhondzadeh et al., 2020; Gérard et al., 2013) have pointed out that, in complex loading polycrystalline cases, the optimal latent hardening coefficients may differ from those derived from single-crystal experiments. Therefore, in the present work, these constants are treated as fitting parameters, with reference values taken from prior literature (Cuitino and Ortiz, 1993).

Grain boundaries will also hinder the dislocation movement and affect the slip resistance; therefore, they are considered in the polycrystalline copper system. Two key mechanisms are considered: the Hall–Petch effect and dislocation accumulation at grain boundaries. The Hall-Petch effect (Hall, 1951; Petch, 1953) quantifies the resistance to dislocation motion as inversely proportional to the square root of the grain size $\bar{D}$. This relationship has been implemented in some VPSC-Type codes (Zhu et al., 2021).

$$\tau_{GB} = k_{slip} \sqrt{1/\bar{D}} \tag{16}$$

Here, k_{slip} is a material constant calculated by the method in (Zhu et al., 2021). The average grain size $\bar{D}$ is calculated based on the EBSD results of undeformed area, approximately 24 μm (Fig. 5). To different samples, tiny changes of $\bar{D}$ are applied due to slightly different grain sizes (Fig. 5). τ_{GB} is treated as constant in the present study.

The dislocation accumulation at grain boundaries is modeled as:

$$\frac{d\rho_{acc}}{d\gamma} = k_{acc} \frac{d\rho_{ann}}{d\gamma} \tag{17}$$

where k_{acc} is the characteristic proportion for dislocation density accumulations and is fitted here (Beyerlein and Tomé, 2008), and ρ_{ann} is the dislocation annihilation term. The overall slip resistance, considering the contribution of dislocation interaction, Hall-Petch effect and the forest hardening, is

finally determined as:

$$\tau_f = \tau_b + \tau_{GB} + c_h Gb\sqrt{\rho_{acc}} \quad (18)$$

3.5. The configurations of the theoretical simulation

In this work, 800 differently oriented grains are configured to form the initial texture of the Cu polycrystalline system, derived from EBSD results and processed using MTEX in MATLAB. The boundary conditions are maintained constant throughout the simulation, ensuring full consistency across all incremental timesteps during the calibration process. A uniaxial tensile strain rate of 5×10^{-3} s^{-1} is applied to replicate the experimental setup, with a strain step increment as 6.5×10^{-6} for 4×10^4 steps in total. Thus, the numerical time integration step is on ~1ms scale. The different current density profiles (Fig. 4) are implemented, while the experimentally observed millisecond-scale variations in synchronous pulsing current time phases (Δt) are also incorporated into the simulations to enhance subsequent comparison with real data. The present simulations incorporated not only information from monocrystals to polycrystals but also achieved temporal precision ranging from milliseconds to minutes scale.

4. Results and discussions

In this Section, we first analyze the mechanical responses and microstructural characterization to provide an overall understanding of the EAD deformation behavior. The crystal plasticity model is then calibrated and validated against the experiments. Section 4.3 examines the simulated evolution of GNDs and SSDs to clarify the dislocation origin of the EAD-induced softening, while Section 4.4, by EC-EVPSC simulations, disentangles the two-stage local stress fluctuations by artificially isolating current effects in the Orowan equation and the dislocation evolution law. Finally, Section 4.5 discusses the physical implications of the proposed mechanism and systematically compares our study with existing ones.

4.1. Experimental results and analysis

This section reports tensile test results, material characterizations and corresponding analysis. First, the number of grains within the EBSD field of view for undeformed samples at 0, 100 and 133 A/mm² is shown in Fig. 6 (5272, 6614 and 4908 grains, respectively). Inverse pole figures (IPFs) along the rolling direction reveal similarly weak textures, while pole figures (PFs) in Fig. S2 (in Supplemantary Materials) display a slight remnant of the typical rolling texture, confirming identical initial textures. Grain size histograms show comparable values (25.65 μm, 24.13 μm and 26.86 μm), ensuring consistency of undeformed microstructures across different loadings.

The tensile test results are presented in Fig. 7. Fig. 7(a) shows engineering stress–strain curves for samples deformed under 0, 100, and 133 A/mm². All specimens reached a maximum engineering strain of 0.3 (~0.262 true strain) without fracture. Slight differences in yield stress arise from minor variations in grain size and initial dislocation density, not from the applied pulse. At $\varepsilon_{true} < 0.002$, the given strain rate and pulse frequency allow at most one pulse, and its energy is insufficient to activate a large amount of local dislocation recovery. Maximum stresses decreased monotonically with current density, with 325, 285, and 266 MPa for 0, 100, and 133 A/mm², respectively. The 40 MPa reduction between the pure mechanical and 100 A/mm² cases exceeds that expected from the temperature-controlled condition in

this study, demonstrating a significant electroplastic effect in pure copper. Justifications to neglect local thermal effects are in Supplementary Materials Part 5.

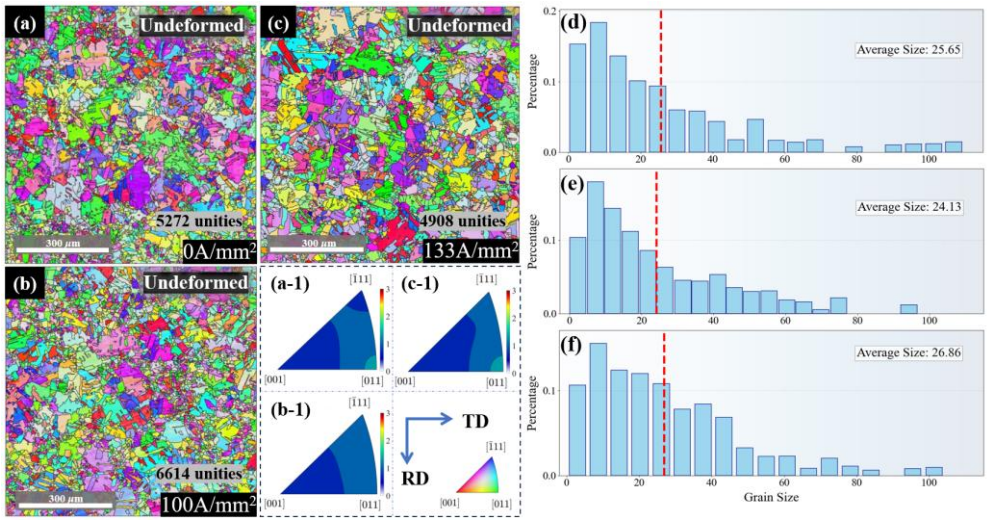

Fig. 6 (a–c) EBSD micrographs of undeformed regions in specimens with current densities of 0, 100, and 133 A/mm², with corresponding inverse pole figures along RD in (a-1), (b-1), and (c-1), showing random crystallographic orientations. (d–f) Grain size histograms from (a–c) reveal comparable distributions and mean values.

Fig. 7 (b) highlights fluctuations in the stress responses: the pure mechanical curve is smooth, whereas 100 and 133 A/mm² curves show periodic variations, increasing in amplitude with current. Fig. 7 (d) details the stress response within a single period of electric pulse with the 133 A/mm² electric density, revealing a characteristic "rapid-slow transition" drop: an initial "rapid drop" within ~35 ms of current application, followed by a "slow decline", and subsequent rebound with hardening after current removal. This behavior, representative of all mechanical response curves, aligns with some reported simulation profiles under one-pulse electric shocking ("instantaneous drop–slow decline") (Dai et al., 2024; Niu et al., 2025; Yan et al., 2023). Under well-controlled temperatures and negligible local heating (see in Supplementary Materials Part 5), the "slow decline" in stress is interpreted as possible accelerated dislocation dynamic recovery induced by electricity (Dai et al., 2024; Tiwari et al., 2022), influencing overall work-hardening rate ($\theta = d\sigma/d\varepsilon$). These observations provide the first detailed experimental observation of individual small stress drops in copper under pulsed EAD.

Fig. 7 (c) presents the overall work-hardening rate to show a decreasing trend with increasing current density. Fig. 7 (c) corresponds to the overall work-hardening of curves in Fig. 7(a). This work-hardening rate is deduced from the envelopes of the fluctuated stress curves, extracted using a Savitzky-Golay filter (Savitzky and Golay, 1964) to smooth out the small fluctuations. The overall work-hardening rate reveals the reduction induced by the current is consistently observed throughout the entire large deformation process. At each strain point in Fig. 7 (c), the relation that $\theta_{J=\ 133A/mm^2}(\varepsilon) < \theta_{J=\ 100A/mm^2}(\varepsilon) < \theta_{J=\ 0A/mm^2}(\varepsilon)$ holds, this denotes the dislocation density accumulations may have been reduced throughout the deformation.

Large-area EBSD was used to check if the applied pulse may have an apparent influence on the deformation mechanism and alter the deformed texture. The EBSD samples are selected in the deformed area (Fig. 2) from the tensile samples after deformation under the current density of 0, 100, and 133 A/mm². The large scan area (1×1 mm²) ensures the texture data is statistically representative. Fig. 8

shows the deformed EBSD maps and IPFs along //RD, with grains elongated along RD and no significant change in size or grain morphology compared to the results of normal mechanical tests (Wang et al., 2022). IPFs reveal <111>//RD peaks typical of polycrystalline copper. Across all current densities, the <111>//RD component remains nearly stable, with only slight increases likely due to sample selection. The <111>//RD pole intensity is not much influenced by EAD process.

Due to recent debates on the activation of non-octahedral slips during EAD (Li et al., 2016; Xu et al., 2022; Xu et al., 2023), futher two-beam TEM characterizations have been implemented to determine dominant ones. TEM shows no abnormal {100}-plane systems activation and such systems are excluded from subsequent simulations. The experimental details are in Supplementary Materials Part 7.

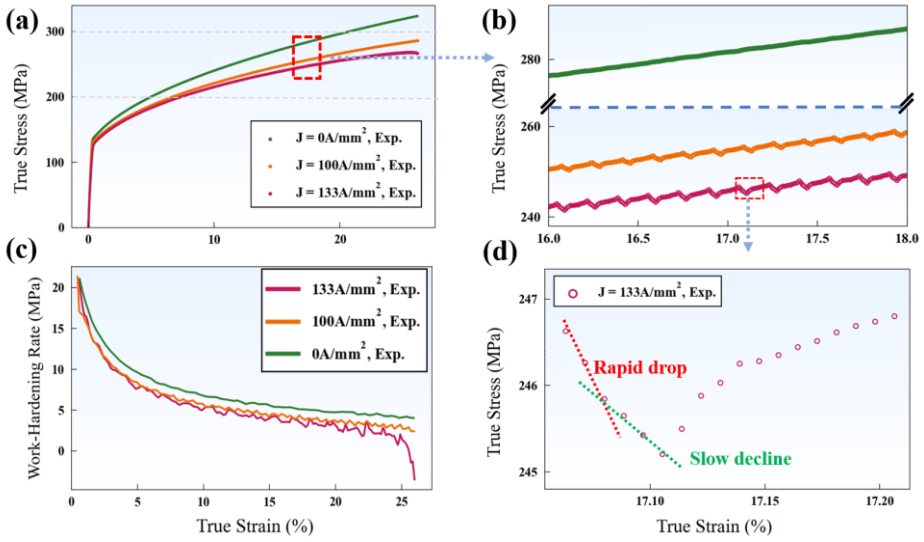

Fig. 7 Stress responses of samples under different pulsed current intensities. (a) Stress–strain curves at 0, 100, and 133 A/mm². (b) Enlarged view showing local fluctuations induced by electricity. (c) Hardening rates under different currents, showing reduced accumulated hardening. (d) Fast and slow drops in stress under pulsing.

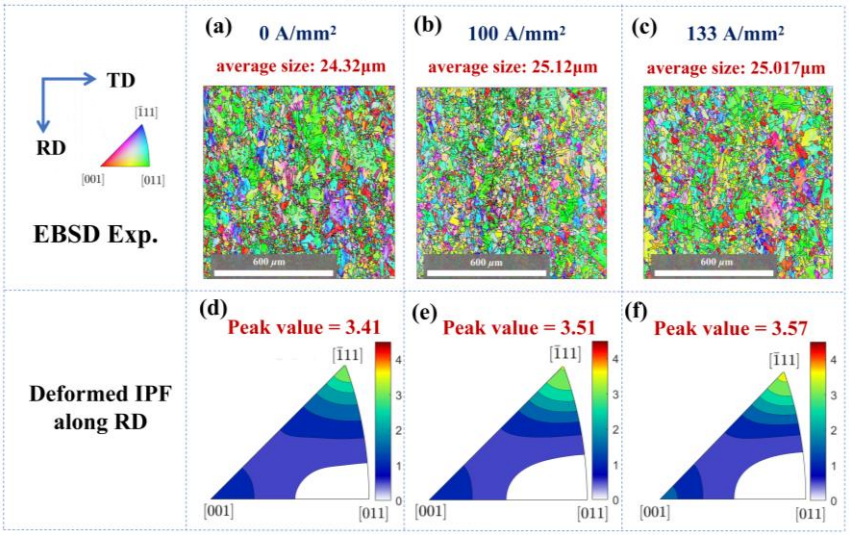

Fig. 8 (a–c) EBSD maps of the deformed areas under different pulsed current intensities. (d–f) IPF maps along the RD axis, derived from the EBSD measurements, showing a quasi-stable intensity.

4.2. Calibration and verification of the self-consistent model

This section presents the calibration and validation of the EC-EVPSC model. Non-electric parameters were fitted using literature data and the stress-strain curve at the electric density J = 0 A/mm², while current-related parameters (J_0 and J_1) were determined from the stress response at J = 100 A/mm². The stress curve at J = 133 A/mm² was then simulated. Quantitative simulations demonstrate the model's ability to reproduce strain-stress responses and deformed textures under different conditions. The quantitative analysis on dislocation density will be demonstrated in Section 4.3.

The parameters for purely mechanical crystal plasticity simulations are listed in Table 2. Classical physical constants, such as the elastic stiffness constant (C_{ij}), shear modulus (μ), and Burgers vector length (b^α) are directly taken from the literature. Other parameters, including v_0, g^α, D^α, τ_c, $h^{\alpha\beta}$, $k_{\rho,mul}$, c_h and $\dot{\varepsilon}_0$ were referenced from previous studies and adjusted for the specific case under consideration. Initial dislocation density on each slip plane (ρ_0^α) and grain-size induced resistance are calibrated systematically to achieve agreement with the measured yield stress. The initial dislocation density and the characteristic proportion for dislocation accumulations (k_{acc}) are aligned with the same order of magnitudes as shown in prior research (Beyerlein and Tomé, 2008; Lei et al., 2025). The parameters obtained following the above procedure are listed in Table 2 below. The slip system considered in this study is the traditional <110> {111} system. Unless otherwise specified, these parameters remain unchanged in subsequent simulations. As shown by the green lines in Fig. 9 (a), the simulated stress-strain curves compare well with pure mechanical experimental data.

Table 2 The model parameters used in CP model.

Parameters	Value and unity	Reference
C_{11}, C_{12}, C_{44}	168.4, 121.4, 75.4 GPa	(Freudenberger and Warlimont, 2018)
μ	46 GPa	(Freudenberger and Warlimont, 2018)
b^α	2.56×10^{-10} m	(Freudenberger and Warlimont, 2018)
g^α	5×10^{-3}	*(Beyerlein and Tomé, 2008)
D^α	370 MPa	*(Beyerlein and Tomé, 2008)
ΔG^α	1.05 eV	(Hull and Bacon, 2011)
τ_c	7 MPa	(Lahiri et al., 2019)
$h_{NJ}, h_{HL}, h_{CJ}, h_{GJ}, h_{SJ}$	1.0, 3.0, 5.0, 5.0, 9.0	*(Cuitino and Ortiz, 1993)
$k_{\rho,mul}$	1.2×10^{8} m^{-1}	(Beyerlein and Tomé, 2008)
v_0	2×10^{2} m·s^{-1}	*(Sun et al., 2024)
c_h	0.097	(Fitted)
$\dot{\varepsilon}_0$	1×10^{7} s^{-1}	(Beyerlein and Tomé, 2008)
ρ_0^α	4.25×10^{12} m^{-2}	(Lei et al., 2025)

τ_{GB}	28 MPa	*(Ghassemali et al., 2015; Zhu et al., 2021)
k_{acc}	0.05	*(Beyerlein and Tomé, 2008)

* This symbol means we only used qualitative relations or calculation methods in these references to fit parameters.

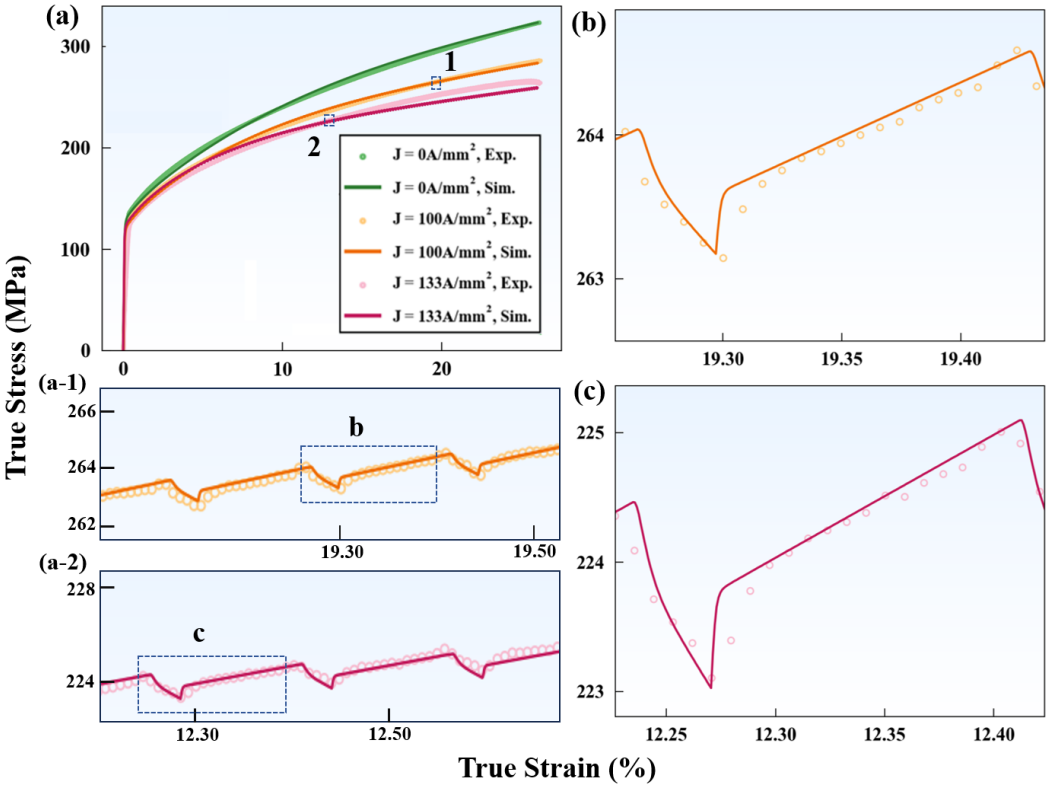

Fig. 9 (a) Experimental (Exp.) and simulated (Sim.) stress-strain curves under various pulsed currents, with two regions (1 and 2) at 100 A/mm² and 133 A/mm² are highlighted. (a-1, a-2) Magnified views of Region 1 and 2 in (a). (b-c) Magnified views of regions **b** and **c**, showing detailed stress responses accurately captured by the EC-EVPSC model.

The model calibration and validation were performed in two steps. First, the electric parameters (J_0 and J_1) were determined by fitting the experimental data at $J = 100$ A/mm². Guided by previous research (Lahiri et al., 2019; Yang et al., 2023a), J_0 is associated with the rapid stress drop. Therefore, it was calibrated against this rapid drop stage. Subsequently, the slow dynamic decline was captured by adjusting J_1 , as this parameter governs the dynamic dislocation recovery in our model (Eq. (13)). Consequently, the entire fitting procedure for a given current density requires information from only a single stress drop event. Further investigation into the deformation mechanisms dominated by these paramters and new insights will be provided in Sections 4.3 and 4.4.

The goal has been to capture both the macroscopic hardening behavior and the local stress fluctuations (as shown in Fig. 9 (a)). To synchronize the simulated pulse phase with the experimental data, a time phase difference introduced by the experiment system of $\Delta t = +5.5$ ms was applied. This synchronization has been validated by the results in Fig. 9 (a-1). Additionally, the initial dislocation density $\rho_0$was slightly adjusted to 3.9×10^{12}m^{-2} to account for minor variations in the experimental yield stress. The difference of the yield stresses (~ 5MPa) falls within the typical uncertainty observed

for different samples of the same material (Niu et al., 2025). Upon calibration, the optimized parameters were determined as $J_0 = 700\text{A/mm}^2$ and $J_1 = 85\text{A/mm}^2$. Fig 10. (b) (the magnified area from Fig. 9 (a)) demonstrates that the calibrated model accurately reproduces the detailed stress responses within a single pulse period.

Subsequently, to validate the predictive capability of the model, these calibrated parameters were applied to the $J = 133\text{A/mm}^2$ case. All material and electric parameters were held constant, with only the time phase difference adjusted to $\Delta t = -9.0\text{ms}$ according to our experiment record to match the experimental phase. As shown in Fig. 9 (a) and (c), the simulation results show excellent agreement with the experimental curve for this higher current density, successfully predicting both the overall stress-strain response and the detailed fluctuation characteristics.

This study marks the first example in which a crystal plasticity model accurately reproduces the local stress–strain response induced by the EAD process. The results offer preliminary validation of the model mechanisms and further highlight the EVPSC framework's capability to predict local stress responses upon changes in loading conditions (Wang et al., 2016; Wang et al., 2010). Fig. 10 demonstrates direct comparisons of the RD-direction IPFs of final textures between the experimental results and simulation results, which also shows consistency. Notably, the <111>//RD intensity remains stable across simulations at different current densities, consistent with experimental observations (see Section 4.3 for further discussion). Although the modeling reproduces the experimental trend quantitatively, it tends to overpredict texture intensity, a well-documented limitation of VPSC-type models (Agnew et al., 2005; Gouriet et al., 2015; Kang et al., 2022). This originates from the classical self-consistent assumption that each grain interacts with a homogeneous effective medium (HEM), causing grains with similar orientations to develop nearly identical plastic responses and texture evolution, whereas in reality each grain is embedded in a heterogeneous microstructural environment where differences in neighboring orientations, morphologies, and constraint conditions play a decisive role in governing its rotation. Thus, the texture intensity may be overpre

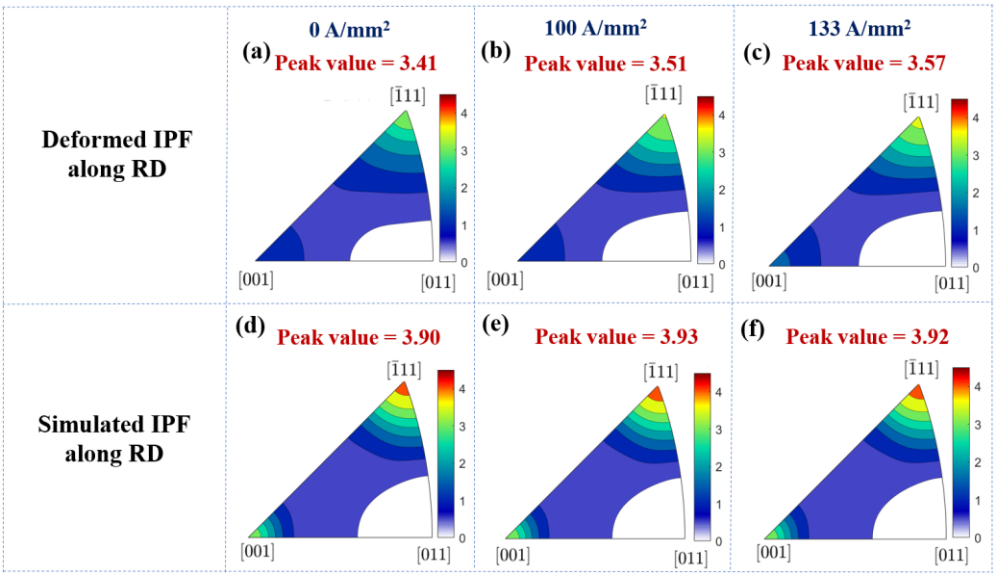

Fig. 10 (a-c) IPF maps along the RD axis, derived from the EBSD measurements. (d-f) Simulated IPF distributions using the EC-SC model, indicating agreement with the experimental observations where the <111>//RD pole intensity increased significantly after tensile tests, demonstrating a typical FCC metal's texture after tensile tests.

To further validate the model's effectiveness, a separate case (J = 70 A/mm²) with a distinct initial grain size (~27 μm) and dislocation density (0.8×10^{12}/m² per slip) was used for verification. The large-area EBSD map, initial IPF along the RD direction (showing weak texture), and initial grain size distribution are provided in Fig. 11 (a-b). All parameters remained unchanged except for the initial dislocation density and the grain-size-related slip resistance to match the initial state of this distinct sample. Fig. 11 (c) shows excellent agreement between the simulated stress curve and the experimental data. Details of the arrow-marked regions are illustrated in Fig. 11 (d-e): Fig. 11 (d) demonstrates the model's consistent accuracy in capturing fine stress fluctuations, while Fig. 11 (e) shows results in another non-overlapping region. Notably, even in this region the model reproduces nearly identical fluctuation features and local slopes, differing only by an ≈2 MPa offset. In Fig. 11(e), the values of local slopes have been indicated inside, obtained by linear regression. $\boldsymbol{k_1}$ and $\boldsymbol{k_1'}$ correspond to the "rapid drop" stage while $\boldsymbol{k_2}$ and $\boldsymbol{k_2'}$ correspond to the "slow decline" one. All these predictive features can validate this model's capability in describing the EAD processes, both in the local fluctuations and the overall hardening features.

Moreover, Fig. 12 presents the IPFs for the validation case, displaying results along RD, TD, and ND. While the RD direction exhibits a consistent pattern with previous findings, the TD and ND directions show excellent agreement with experimental data. In addition, the grain size has not been changed after EAD, consistent with the observation and analysis in Section 4.1. These results furtherly validate that the model effectively captures the texture evolution of copper during the EAD process. An additional validation case under current density

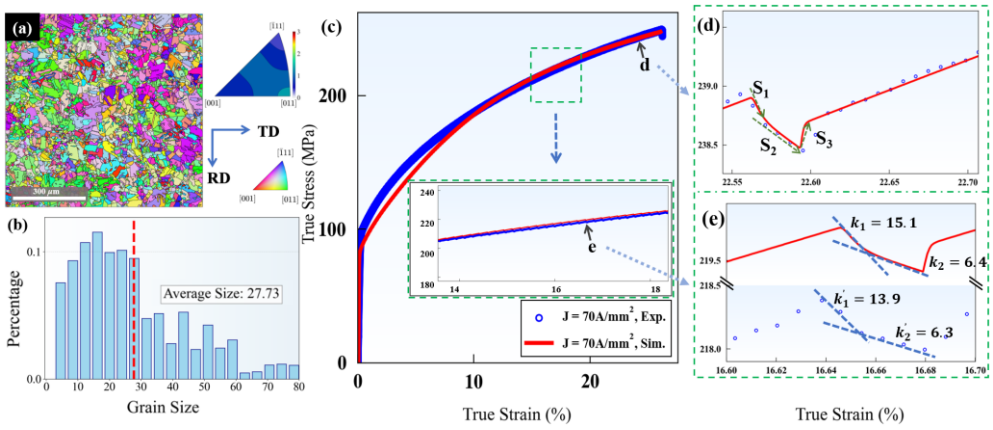

Fig. 11 (a-b) EBSD grain image of the undeformed sample and initial grain size distribution before deformation. (c) Experimental (Exp.) and Simulated (Sim.) stress–strain curves under a pulsed current density of 70 A/mm² and an initial dislocation density of 0.8×10^{12}/m² in each slip system, validating the accuracy of the calibrated model. (d) Magnified view of the stress–strain response during several electric pulses. (e) Quantitative agreement of the stress evolution during the rapid drop, slow drop, and post-current lift stages within a single pulse.

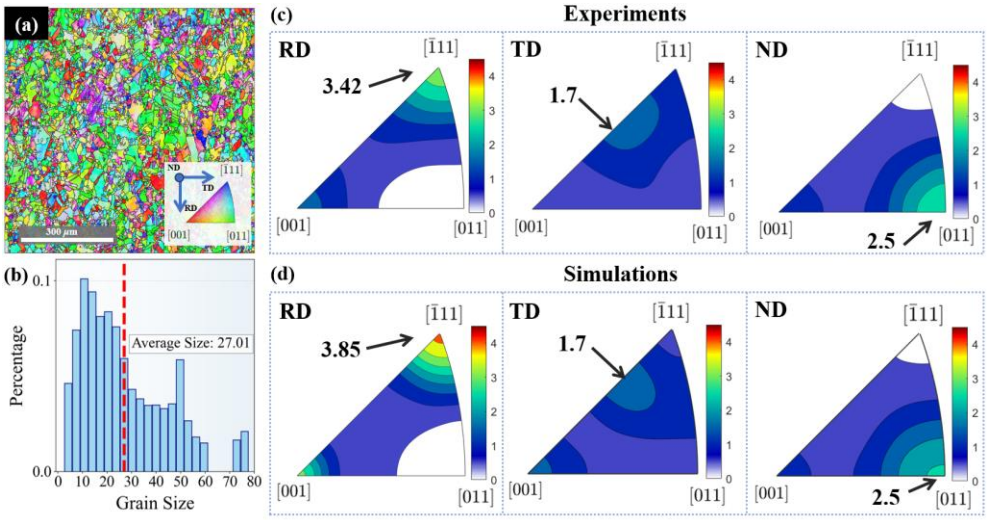

Fig. 12 (a) EBSD grain image of the deformed sample. (b) Grain size distribution, showing minimal change from the undeformed region. (c-d) Experimental and simulated IPFs along RD, TD, and ND; arrows indicate peak pole intensities. Qualitative comparison shows the model reproduces the deformed texture well.

In Appendix 5, we present a further validation conducted under operating parameters of a 10% duty cycle, 1 Hz frequency, and 133 A/mm² current density. The satisfactory agreement in the macroscopic stress-strain comparison and the details shown in the magnified views demonstrate the robustness of the model under different loading conditions.

4.3. Dislocation density evolutions and grain orientations

In this section, simulation results on dislocation density evolutions and corresponding full-field HR-EBSD evaluations are presented, revealing current-induced dislocation recovery. The dislocation density evolutions under pulsing currents feature local fluctuations linked to current intensity and true strain. Analysis on SSDs and GNDs is also incorporated inside for further discussions on grain orientations and previously demonstrated texture results. The total dislocation density evolution is computed via a volume-weighted average of the density within each individual grain.

Fig. 13 (a-b) show the simulated dislocation evolutions under three different current densities throughout the deformation. Fig. 13 (a) shows the overall tendency, with significant differences observed that the densities decrease as the applied current increases. Fig. 13 (b) shows an enlarged view for the boxed area inside Fig. 13 (a) for more details: the small fluctuations show the dislocation recovery raised by the applied pulses. The inserted image inside Fig. 13 (b) presents the detail of the boxed area, showing that the amplitude of these fluctuations is positively correlated with the current density. The slopes of the decreasing stages in 100 A/mm² and 133 A/mm² cases are denoted as k_{100} and k_{133}. It is obvious that $k_{133} < k_{100}$, indicating the dislocation recovery in one pulse increases with the applied current density.

To quantitatively analyze these “small recoveries”, Fig. 13 (c) provides the amplitude of the recoveries at certain true strain extents. Obviously, the larger the input current density is, the stronger the local recovery is. Besides, the increasing trend indicates that a single current pulse can induce greater dislocation recovery at higher strain extents, where more dislocations are already present. This trend suggests that the electroplastic effect not only depends on the current density, but also becomes more

pronounced with a higher amount of the stored dislocation density, consistent with prior studies (Bilyk et al., 2005; Kim et al., 2017).

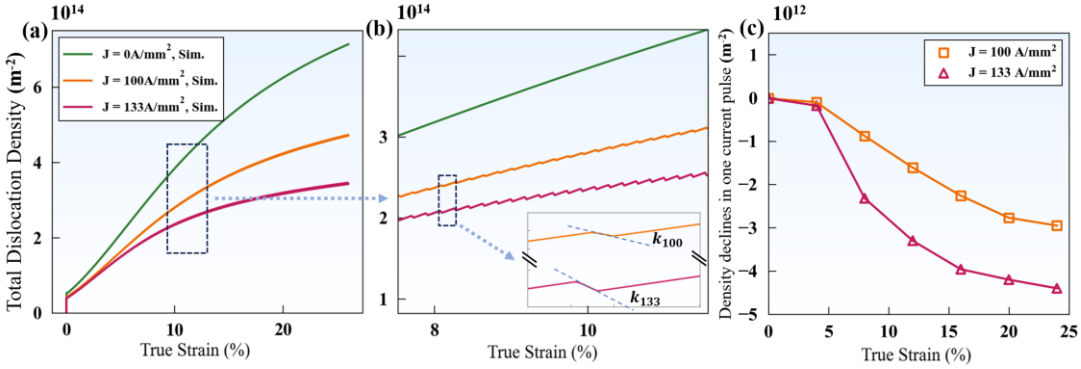

Fig. 13 (a) Simulated total dislocation density evolution. (b) Enlarged view of the boxed region showing rises and drops under pulsed currents; inset highlights density declines at different currents. (c) The plot of dislocation density declines in each pulse period versus true strain under different current density.

To verify the dislocation density recovery magnitude, high-resolution EBSD (HR-EBSD) coupled with the Williamson-Hall (WH) method (Borbély, 2022) was employed to analyze the dislocation increment ratio r_{tot}, defined as the ratio between the final total DD and the initial total DD ($r_{tot} = \rho_{total\_final}/\rho_{total\_init}$). During the r_{tot} evaluation procedure, 4×10^4 Kikuchi patterns recorded by EBSD experiments are used. The transversal brightness profiles of major Kikuchi bands are extracted (Takeuchi et al., 2025) and compared with those of simulated diffraction patterns. A dedicated diffraction signal correlation method is used to characterize the blurriness of the experimental diffraction patterns, represented by the kernel size of the Gaussian function convolution. The slope of the kernels of convolution functions is transformed into relative dislocation densities ($r_{tot} = \rho_{tot\_final}/\rho_{tot\_init}$). The measured kernel angle misorientation (KAM) values are converted into GNDs densities ($r_{GND} = \rho_{GND\_final}/\rho_{GND\_init}$) by methods in (Zhong et al., 2024). Since HR-EBSD provides full-field measurements, the SSD density can be directly mapped through the subtraction $\rho_{SSD} = \rho_{tot} - \rho_{GND}$ at each pixel. This procedure firstly gives ρ_{GND} and ρ_{tot} (thus r_{GND} and r_{tot}), and yields ρ_{SSD} (thus r_{SSD}) accordingly.

Fig. 14 (a) shows the reported dislocation density evolution along with experimental data from the literature, showing great consistency with the non-electric case, which validates the simulations in Section 4.2. (Čebron and Kosel, 2014; Zehetbauer and Seumer, 1993). The initial and deformed dislocation densities in the case J = 100 A/mm^2 estimated by HR-EBSD is also provided as orange markers. The deformed dislocation density is obtained by aligning the initial value to the simulation configuration and multiplying by the final-to-initial ratio r_{tot} derived from the post-processed EBSD maps in Fig. 14 (b-c). Error bars reflect the statistical distributions within these maps. Fig. 14 (d) shows a quantitative comparison of r_{tot} for three simulation cases and one experimental case. Beyond confirming the prediction-experiment consistency, the results quantitatively demonstrate electricity-induced dislocation recovery and its dependency on the electric density.

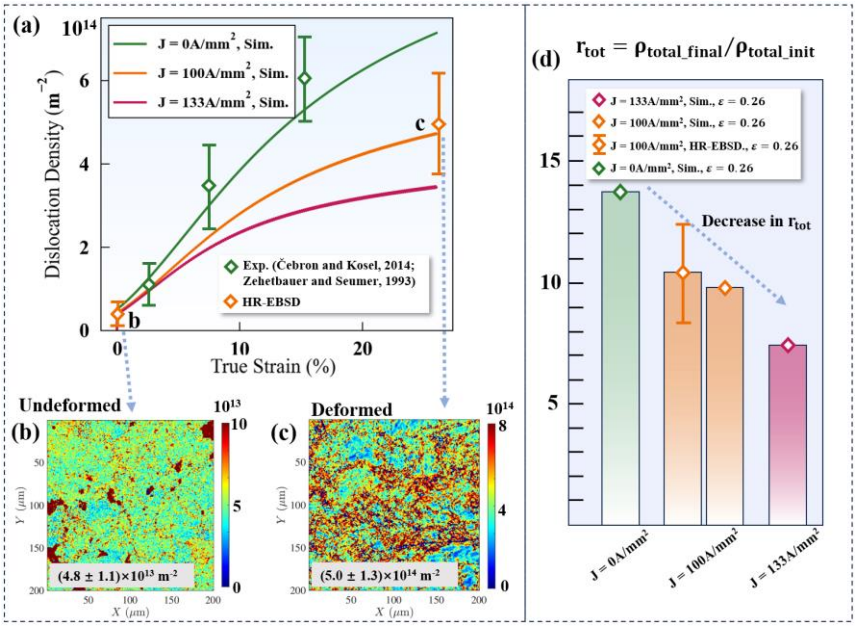

Fig. 14 (a) For quantitatively illustrating the validation of our dislocation density evolution curve. Presented here are several works on the densities of copper (Čebron and Kosel, 2014; Zehetbauer and Seumer, 1993) and the value measured in our work by HR-EBSD. (b-c) The undeformed and deformed full-field total DD distribution image with mean values indicated. (d) Histogram of $\rho_{total\_final}/\rho_{total\_init}$ comparison of simulation under different current densities (0 A/mm^2, 100 A/mm^2 and 133 A/mm^2) and HR-EBSD results under 100 A/mm^2.

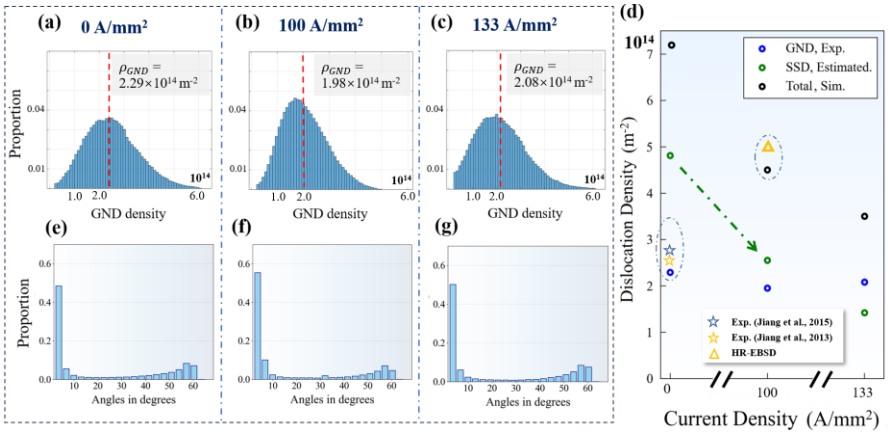

Fig. 15 (a–c) Histograms and average values of GND densities deformed under different pulsed currents. (d) Total dislocation, GND, and estimated SSD densities versus pulsed current; pentagons indicate GND values at the same strain (~26%) from conventional tensile tests (Jiang et al., 2013; Jiang et al., 2015). To avoid ambiguity, each dashed ellipse represents the same value measured or calculated in different methods or studies. (e–g) Stable grain misorientation distributions of samples corresponding to (a–c).

In the EC-EVPSC model, a conventional dislocation density-based homogenization framework, GNDs and SSDs are not computed separately; only the total dislocation density is tracked. To identify the individual contributions, the EBSD data in Fig. 8 were converted into GNDs (shown in Fig. 15a–c) using the classical Ashby relation ($\rho_{GND} = \beta KAM/Lb^{\alpha}$) (Ashby 1970; Shi 2021) where we take $\beta =$

3 (Konijnenberg et al., 2015) and $L = 1.0$ μm. The simulated SSD was then obtained by subtracting the GND from the total dislocation density. Fig. 15 (d) presents the total dislocation density, GND, and SSD at the end of deformation (ε = 0.26) for various current densities. The GND appears largely unaffected by the applied current across deformation conditions, whereas the SSDs show significant differences. Notably, SSDs primarily contribute to strength through random pinning (Arsenlis and Parks, 1999), and GNDs are responsible for accommodating lattice curvature (Gao and Huang, 2003) and driving grain rotation (Liang and Dunne, 2009). Fig. 15 (e-g) show that grain misorientation distributions of different samples possess no significant difference. This explains the texture results: in copper, the electroplastic effect primarily incorporates the recovery of SSDs rather than GNDs, thus maintaining a quasi-stable <111>//RD fiber intensity.

4.4. Electro-mechanical coupled mechanisms controlling the overall electroplastic effects

Previous studies revealed a two-stage local stress response ("rapid drop" and "slow decline") linked to dislocation movements under electro-mechanical coupling. This section examines the mechanisms by introducing pulsed electricity separately into the Orowan equation and the modified Kocks-Mecking model, isolating their contributions to the observed responses in experiments and simulations. Note that this is only a modeling demonstration, with all parameters identical to the J = 0 A/mm² case.

Simulations are first performed with dislocation evolution laws disabled (Section 3.3), retaining only the current-dependent terms in the Orowan equation (Section 3.2) representing short-range barrier reduction. This mathematical form that only considers EAD's influence on Orowan equations, also used in CPFEM studies (Lahiri et al., 2019; Yang et al., 2023a; Zheng and Yi, 2025), shows no clear effect of current density on the stress-strain envelope (Fig. 16a), aside from local stress fluctuations and "rapid drops" (Figs. 16a-1, 16a-2). As Fig. 16 (b) indicates, dislocation evolution is unchanged, explaining the invariant stress-strain envelopes. Thus, the Orowan equation alone explains only the "reversible" stress reductions in EAD and shows no cumulative effects. However, even without changes in dislocation density, the stress drops in these cases increase slightly with tensile strain, consistent with experimental observations. To clarify this behavior, an analysis is conducted on the relationship between current "density (J) - true strain (ε) – magnitude of rapid stress drop ($\Delta\sigma$)". This analysis follows prior studies (Lahiri et al., 2019; Molotskii and Fleurov, 1995) with some mathematical modifications. The quantitative relationship is given directly below, with justifications in Appendix 2:

$$\Delta\sigma(J) = M\tau_c^{\alpha}\frac{J^2}{J_0^2}\Big/\left(1+\frac{J^2}{J_0^2}\right) \tag{19}$$

where M is the Taylor factor (Lahiri et al., 2019) of the activated slip system. The rapid stress drop ($\Delta\sigma$) at 11% and 25% strain (Fig. 16 (c)) increases with current and rises slightly with strain. The fitted Taylor factor increased a little, reflecting the behavior mainly governed by the strengthening of the <111>//RD texture (Gao et al., 2022): as more {111} plane normals align with the tensile axis, the M increases and the slip velocity on {111} planes becomes higher. At larger strains, maintaining a constant macroscopic strain rate under sudden current requires greater instantaneous changes in ΔG_0^{α} and τ_c^{α}, which enhances $\Delta\sigma$. Thus, $\Delta\sigma$ scales positively with strain even under same current density. This also implies that in EAD processes with lower Taylor factors (e.g., torsion, $M \approx 1.7$) or extreme textures (e.g., copper wires), the electroplastic effect may be different.

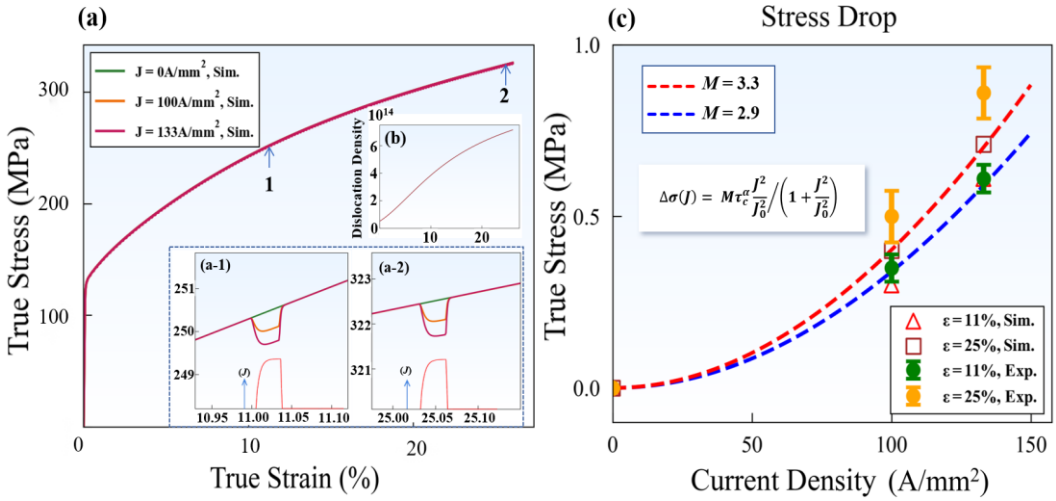

Fig. 16 (a) Stress responses from electricity-coupled dislocation movement under different currents. (a-1, a-2) Enlarged views showing rapid stress drops with normalized current profiles. (b) Dislocation density evolution for three curves, showing no change during deformation under different currents. (c) Stress drops versus current density, compared with theoretical predictions from the Orowan equation and experimental values with error bars.

Following a discussion on the relationship between "rapid drop" and the electricity-affected Orowan equation, additional simulation cases are conducted without electroplasticity on the Orowan equation (Section 3.2) and with the modified dislocation evolution law activated (Section 3.3). The red markings in the equation of Fig. 17 indicate how current influences the modified Kocks–Mecking relationship. In Fig. 17(b), the stress curve shows the earlier "work-softening" behavior without any rapid drop, and Fig. 17(c) shows dislocation density evolution similar to before, with $\mathrm{sgn}(d\rho/d\gamma)$ from positive to negative rapidly at the rising edge of the pulses. These results clearly show how the electricity affects the dislocation dynamic recovery, therefore providing the "slow decline" phase in the local stress fluctuations. The density declines in each pulse evolving with tensile strain have been discussed in Section 4.4.

Two points should be noted here. First, the modification of $k_{\rho,mul}$ mathematically corresponds to multiplying the right-hand side of the dislocation evolution law by a factor smaller than 1.0. This alone will not result in a positive to negative change of the $\mathrm{sgn}(d\rho/d\gamma)$ but only lower down the multiplication rate. Second, to reproduce the 'work-softening' behavior before and after the applied pulses, as well as dislocation evolution rates of opposite signs, an influence on g^{α} must be incorporated. The modification of g^{α} arises from the electron–dislocation scattering mechanism, indicating its dominant role in the electroplastic dislocation dynamic recovery process. This modification is consistent with arguments of previous studies on copper (Dai et al., 2024; Li et al., 2013). On the other hand, even if the modification of g^{α} is disabled and only $k_{\rho,mul}(J)$ is retained, the decrease in macroscopic work-hardening rate can still be ensured. The second effect explains why some studies (Xu et al., 2022; Zheng and Yi, 2025) can capture changes in macroscopic work-hardening solely by incorporating changes in mean free path length.

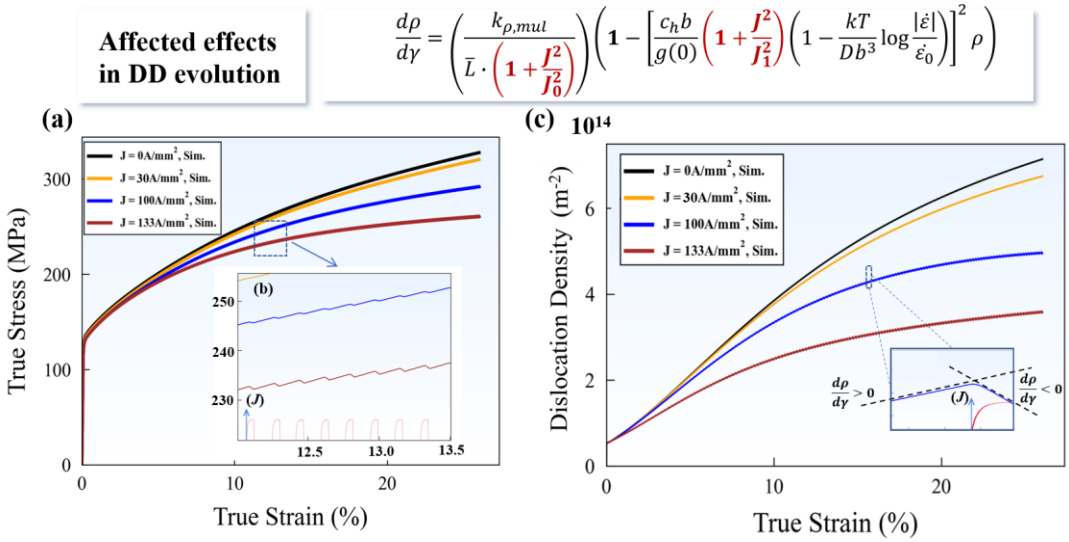

Fig. 17 (a) Stress responses governed by electricity-coupled dislocation evolution under different currents. (b) Enlarged view showing the slow stress drop with increasing current. (c) Dislocation evolution curve with fluctuations induced by periodic electric pulses, showing electric-induced dynamic recovery process.

To make a summary, local fluctuation in stress responses during EAD is divided into three stages (S1–S3, Fig. 18): rapid drop (S1) from short-range barrier reduction (Fig. 18 (b)), dynamic recovery process (S2) via electric-induced dislocation motion (Fig. 18 (c)), and rebound (S3) from new displacement multiplication and reverse of short-range barrier (Fig. 18 (d)). The transition from S1 to S2 occurs at the characteristic time of the current pulse (τ_t). If $\tau_t \to 0s$, which means a perfect square wave profile, a perfect "instantaneous drop" could be expected. The overall work-hardening arises from the cumulative effect of these stages. However, different FCC metals, even with similar stacking fault energies (e.g., Al vs. Ni), show distinct electroplastic effects (Kim et al., 2017; Liang et al., 2017; Yan et al., 2023; Zhang et al., 2020), indicating that the mechanisms controlling electroplastic effects operate at a finer scale than that at which stacking fault energy, activation energy, and slip resistance are typically defined. More discussions will be presented in Section 4.5.

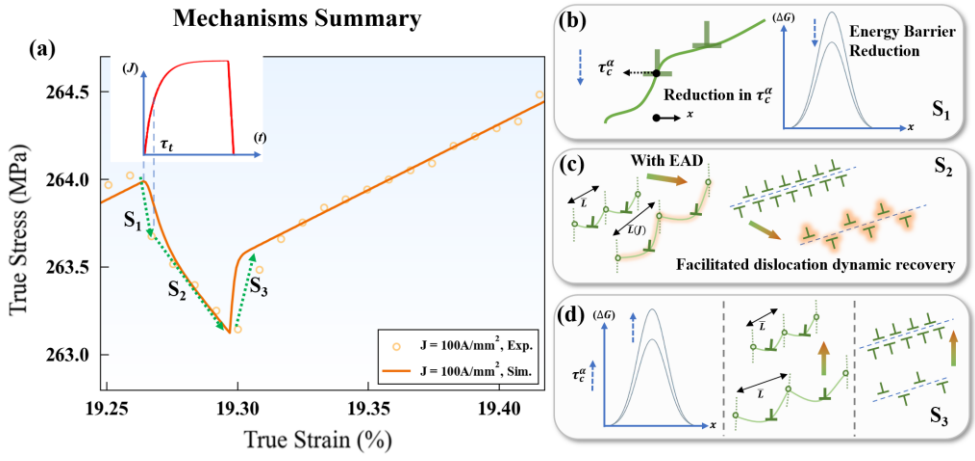

Fig. 18 (a) The 3-stage stress response in a single pulse, with the pulse profile accompanied. (b-d) The schematic figures of the mechanisms in the 3 stages. This abstract for mechanisms highlights the

differences between the instantaneous barrier reduction and the subsequent dynamic process.

4.5. Revisiting previous studies

Building on the above discussion of the key mechanisms of electroplastic effects in copper, several classic studies on electroplasticity warrant revisiting and re-examination, as they may offer new insights into earlier findings.

Previous studies on copper under electric-assisted deformation (EAD) have shown reductions in maximum flow stress and work-hardening (He et al., 2020; Xu et al., 2022; Zhang et al., 2018). Our temperature-controlled experiments confirm these findings, with stress-strain curve envelopes and crystal plasticity simulations indicating suppressed dislocation multiplication. For samples with similar grain sizes, (Zhang et al., 2018) reported only minor yield-stress variations under different current densities and our results are consistent with this trend. Current-induced stress drops, long recognized in literature (Li et al., 2013; Silveira et al., 1981; Zhang et al., 2018), are also observed here, providing further evidence of electroplastic stress-strain responses and their relation to dislocation density evolution. In contrast, texture evolution differs from some earlier reports. EBSD studies (Xu et al., 2022) suggested a reduction of <111>//RD intensity and ~10% loss of <111>-oriented grains, but large-area EBSD in the present study reveals no such weakening, implying that earlier conclusions may reflect limited mapping fields. At the dislocation scale, TEM analysis of the {100} <110> system indicates that non-octahedral slip is unlikely to be activated, as evidenced by its low dislocation density, isolated morphology, and the absence of corresponding texture evolution. It has been attributed to Lomer–Cottrell locks, known to contribute to copper's hardening (Anderson et al., 2017), and does not support the presence of enhanced non-octahedral activity suggested in previous work.

Furthermore, new interpretations can be proposed for the counterexample reported by (Rudolf et al., 2021), where copper exhibited electroplastic effects only in maximum elongation but not in work hardening. In that study, EAD tests were carried out under continuous direct current (CDC) conditions at very low strain rates, with loading times of up to 40 minutes before fracture. Notably, before yielding, there was an initial loading period of about one minute, sufficient for CDC to directly annihilate dislocations (Zhang et al., 2020). The yield stress is thus changed. The magnitude of dislocation density annihilated in this process could be roughly estimated by the Taylor relation (Taylor, 1934) that $\Delta\sigma \sim \alpha\mu b\Delta\sqrt{\rho}$. Taking $\alpha \approx 0.4$ (Akhondzadeh et al., 2020; Madec et al., 2002) and $\Delta\sigma = 15$ MPa (Rudolf et al., 2021), this estimation yields a dislocation density change of $\Delta\sqrt{\rho} \approx 3 \times 10^6\ m^{-1}$. By supposing an initial dislocation density as $\rho_0 = \sum_\alpha \rho_0^\alpha \approx 10^{14} m^{-2}$ (Lei et al., 2025) and noting the real initial density as ρ_{real}, we could have that: $\Delta\sqrt{\rho} = \sqrt{\rho_0} - \sqrt{\rho_{real}} \approx 3 \times 10^6\ m^{-1}$ and thus $\rho_{real} \approx 0.5 \times 10^{14} m^{-2}$ which accounts for a half of ρ_0. This magnitude suggests that the electroplastic effects are not significant due to the pre-annihilated dislocations. In addition, starting temperature of TAD loading to compare the J = 125 A/mm^2 case deviated clearly from the room temperature, showing a possible long pre-loading period with temperature rising and thus initiated dislocation recovery.

In addition to conventional experiments, since the 1980s (Silveira et al., 1981), researchers have attempted to eliminate thermal effects in electroplastic experiments using liquid helium or nitrogen, a method still used today (Zhao et al., 2021). One study tested Pb (an FCC metal) (Silveira et al., 1981) at 4.2 K during EAD and reported no electroplastic effect, long regarded as evidence that electroplastic

arises solely from the Joule effect. This interpretation is flawed. As a Type-I superconductor (Kittel and McEuen, 2018), Pb follows BCS theory (Bardeen et al., 1957a; Bardeen et al., 1957b), where Cooper pair formation suppresses electron-lattice scattering, drastically reducing momentum transfer. Additionally, the Meissner effect (Meissner and Ochsenfeld, 1933) limits magnetic field penetration, hindering magnetoplastic mechanisms. Later studies (Molotskii, 1995; VA, 1997) highlighted magnetic field effects, while more recent work (Dai et al., 2024; Lahiri et al., 2019; Li et al., 2013; Niu et al., 2025; Xu et al., 2022) emphasized electron-dislocation scattering. Thus, the 'null-electroplastic' effect likely reflects an artifact from suppressing mechanisms (electron-dislocation scattering and magnetoplasticity) of electroplastic under superconductivity.

Lastly, another key factor influencing electroplastic effects is the type of metal, as discussed in Section 4.4. For example, the quantitative contribution of electron-dislocation scattering also depends on intrinsic material properties, as the electron relaxation time τ_{relax} varies across metals and can be expressed explicitly (Xu et al., 2023).

$$\frac{1}{\tau_{relax}} = \frac{1}{\tau_{cry}} + \frac{1}{\tau_{dis}} \tag{20}$$

where τ_{cry} and τ_{dis} are the relaxation times for perfect lattices and dislocations depend on the material type and the atomistic level electronic structure. The energy ΔE transferred by drifting electrons scales as $\Delta E \propto {\tau_{relax}}^2$ (Dai et al., 2024; Li et al., 2013). Accordingly, J_1 and J_0 are treated as fitting parameters to capture material-dependent electroplastic responses. These physical facts highlight the difficulty of establishing a unified electroplasticity model applicable to all materials. Modeling and analysis of other FCC metals (e.g., pure aluminum) are beyond the scope of this work and will be reported separately in another work.

5. Conclusions

This study provides new experimental and modeling insights into the electroplasticity of copper under pulsed current EAD loading. The main conclusions can be summarized as follows:

(1) Temperature-controlled experiments demonstrated pronounced electroplastic effects in copper subjected to pulsed currents, manifested by significant reductions in maximum tensile stress and work-hardening rate. These results provide direct evidence of athermal contributions beyond conventional thermal softening. The stress-strain curves under EAD loading exhibited characteristic stress fluctuations, with the local response showing "rapid drop" and "slow decline" phases, in contrast to the smooth profiles in purely mechanical deformation response.

(2) Large-area EBSD (1000 μm × 1000 μm) and two-beam TEM analyses confirmed that copper under EAD deforms primarily via conventional {111} <110> slips, with no significant non-octahedral activation. Textures and grain misorientation distributions for deformed samples in different EAD cases retained well, indicating slight current-induced orientation changes. HR-EBSD and EC-EVPSC simulations consistently showed a marked reduction in total dislocation density under current, mainly from annihilation of statistically stored dislocations (SSDs), while geometrically necessary dislocations (GNDs) remained nearly stable.

(3) The EC-EVPSC model successfully reproduced temporal electricity-induced stress-strain responses, dislocation density evolution, and texture stability, demonstrating strong predictive

capability and providing a fast and robust experimental-numerical framework for exploring electroplastic mechanisms. The satisfactory predictions rely on the necessity of coupling the electricity-related term with the thermodynamic evolution laws. By addressing the physical origins, the efficiency of this treatment is highlighted by the fact that only two electricity-related parameters (J_0 and J_1) are required to capture these complex mechanisms, distinguishing the present approach from phenomenological fitting.

(4) The local responses on stress-strain curves could be decoupled into three stages (S1, S2 and S3), attributed respectively to instantaneous friction barrier drop (S1), promoted dislocation recovery and changes in mean free paths (S2), and subsequent dislocation multiplications and barrier recovery (S3). Essentially, the divergence in the stress-strain envelopes and work-hardening rates represents the collective outcome of these local stress drops stimulated during EAD experiments.

Beyond the specific conclusions, this work highlights a mechanism-focused perspective on electroplasticity in copper under pulsed-current loading. By integrating established electroplastic mechanisms within a dislocation-density-based framework, the study enables interpretations of how athermal contributions influence macroscopic softening. Further semi-quantitative evalution is achieved by integrating model predictions with HR-EBSD evidence. This combined approach effectively and synergistically linked the microscopic mechanisms with observed stress-strain responses, providing a concise, physics-based understanding that may guide further exploration and modeling of electroplastic deformation in metals.

Appendix 1. The self-consistent scheme of EVPSC model

The core mathematics involves volume-weighted averaging of grain-level stretching rate (d_{ij}), rotation rate (w_{ij}), and Cauchy stress (σ_{ij}) tensors into macroscopic quantities, as shown in Eq. (2). Here, the capitals indicate corresponding macroscopic quantities (ex. D_{ij} denotes macroscopic stretching tensor) and lower-case letters represent the grain level ones.

$$D_{ij} = D_{ij}^{e} + D_{ij}^{p} = \frac{1}{V}\int (d_{ij}^{e} + d_{ij}^{p})\, dV \tag{A1a}$$

$$W_{ij} = W_{ij}^{e} + W_{ij}^{p} = \frac{1}{V}\int (w_{ij}^{e} + w_{ij}^{p})\, dV \tag{A1b}$$

$$\Sigma_{ij} = \frac{1}{V}\int \sigma_{ij}\, dV \tag{A1c}$$

The notation e and p denote elastic and plastic parts. The material's elastic behavior relates the Jaumann rate of the Cauchy stress $\dot{\Sigma}_{kl}^{\nabla}$ and $\dot{\sigma}_{kl}^{\nabla}$ to the elastic stretching rate. The nonlinear viscoplastic strain rate is expressed pseudo-linearly with stress (Nemat-Nassar et al., 2012), combining with the strain tensor d_{ij}^{0} and D_{ij}^{0}:

$$D_{ij} = \bar{M}_{ijkl}^{e}\dot{\Sigma}_{kl}^{\nabla} + \bar{M}_{ijkl}^{p}\Sigma_{kl} + D_{ij}^{0} \tag{A2}$$

$$d_{ij} = M_{ijkl}^{e,g}\dot{\sigma}_{kl}^{\nabla} + M_{ijkl}^{p,g}\sigma_{kl} + d_{ij}^{0} \tag{A3}$$

M_{ijkl}^{e} and M_{ijkl}^{p} are respectively the elastic compliance tensor and plastic compliance (Wang et al., 2010). The 'overbar' indicates the compliance in the polycrystal scale system. The localization factor B_{ijkl}^{g} and back stress tensor b_{ij}^{g} connect the viscoplastic behavior of individual grains to the

macroscopic polycrystal response, applicable to both elastic and plastic parts (Wang et al., 2010). The notation g denotes 'grain level'.

$$\sigma_{ij} = B^{g}_{ijkl}\Sigma_{kl} + b^{g}_{ij} \tag{A4}$$

The plastic deformation gradient tensor l^{p}_{ij} in each grain is controlled by dislocation-induced plasticity and twinning behavior is not included in this study:

$$l^{p}_{ij} = l^{dis}_{ij} \tag{A5}$$

Note that the average elastic and plastic compliance $\overline{M}^{e,p}_{ijkl}$ is defined in a polycrystal system but is not equal to the volume-weighted average. The 'self-consistent' process involves solving linear systems about components of compliance tensors and localization tensors, which could be yielded by substituting Eqs. (A2)-(A5) into (A1), thus enabling the final solution of multiscale constitutive laws. This approach is typically faster than CPFEM, as it avoids the need for complex meshing.

Appendix 2. Estimation of electrically influenced "rapid drop"

2.1. Derivation of the quantitative relationship

The relationship between "current density (J) - true strain (ε) – magnitude of rapid stress drop ($\Delta\sigma$)" is presented here. This analysis is analogous to the ones in prior research (Lahiri et al., 2019), but with some differences in mathematical form. We link the bulk plastic behavior to that of an individual grain through the Taylor factor (M) of the activated slip system and treat the macroscopic and slip level plastic strain rate as a function of current density: $\dot{\varepsilon}_p(J)$ and $\dot{\gamma}^{\alpha}(J)$, which gives:

$$\dot{\varepsilon}_p(J) = \frac{1}{M}\sum_{\alpha}\dot{\gamma}^{\alpha}(J) = \frac{1}{M}\sum_{\alpha}\dot{\gamma}^{\alpha}_0 \exp\left(\frac{-\Delta G^{\alpha}(J)}{k_B T}\right) \tag{A6}$$

where $\Delta G^{\alpha}(J) = \Delta G^{\alpha}_0 \Big/ \left(1+\frac{J^2}{J_0^2}\right)\left[1-\frac{\sigma_{eff}(J)/M}{\tau^{\alpha}_c}\left(1+\frac{J^2}{J_0^2}\right)\right]$. Here, we neglect the elastic strain rate $\dot{\varepsilon}_e$, with detailed justifications for this neglection in Appendix 2.2. Thus, we suppose that the imposed loading boundary condition ($\dot{\varepsilon}(0) = \dot{\varepsilon}(J) = 5\times10^{-3}$ s^{-1}) gives directly that $\dot{\varepsilon}_p(0) = \dot{\varepsilon}_p(J)$. By imposing $\dot{\varepsilon}_p(0) = \dot{\varepsilon}_p(J)$, we get:

$$\frac{1}{M}\sum_{\alpha}\dot{\gamma}^{\alpha}_0 \exp\left(\frac{-\Delta G^{\alpha}(J)}{k_B T}\right) = \frac{1}{M}\sum_{\alpha}\dot{\gamma}^{\alpha}_0 \exp\left(\frac{-\Delta G^{\alpha}(0)}{k_B T}\right), \quad \forall J>0, \alpha \in \{1,2,..,12\}$$
$$\Rightarrow \Delta G^{\alpha}(0) = \Delta G^{\alpha}(J) \tag{A7}$$

from which we get:

$$\Delta G^{\alpha}_0 \Big/ \left(1+\frac{J^2}{J_0^2}\right)\left[1-\frac{\sigma_{eff}(J)/M}{\tau^{\alpha}_c}\left(1+\frac{J^2}{J_0^2}\right)\right] = \Delta G^{\alpha}_0\left[1-\frac{\sigma_{eff}(0)/M}{\tau^{\alpha}_c}\right] \tag{A8}$$

From the above expression, we obtain:

$$\sigma_{eff}(J) - \sigma_{eff}(0) = -M\tau^{\alpha}_c \frac{J^2}{J_0^2}\Big/\left(1+\frac{J^2}{J_0^2}\right) < 0 \tag{A9}$$

Eq (A9) actually predicts a stress "drop" upon sudden current excitation due to its negative property. Here, we define the absolute value of the drop as $\Delta\sigma_{eff} \overset{\text{def}}{=} \text{abs}(\sigma_{eff}(J) - \sigma_{eff}(0))$. The $\Delta\sigma_{eff}$ could

also be expressed as $\Delta\sigma_{eff} = \Delta\sigma - \Delta\sigma_{friction}$. The equivalent friction stress $\sigma_{friction}$ is defined as: $\sigma_{friction}(J) \triangleq M\tau_f = M\left(\tau_b + \tau_{GB} + c_h Gb\sqrt{\rho_{acc}}\right)$, which is a function of dislocation density and grain size. Due to no change in dislocation density and grain size in the analysis in Section 4.4, $\Delta\sigma_{friction}(J)$ is imposed to 0 and we get $\Delta\sigma_{eff} = \Delta\sigma(J)$. Thus, we obtain the quantitative relationship between current density and rapid stress drops, with M related to true strain, noted as $M(\varepsilon)$.

$$\Delta\sigma(J) = M(\varepsilon)\tau_c^{\alpha}\frac{J^2}{J_0^2}\Big/\left(1+\frac{J^2}{J_0^2}\right) \tag{A10}$$

The stress drops at different strains and current densities are analyzed in detail in Section 4.4.

2.2 Justifications for neglecting elastic strain rate

The total strain rate of uniaxial tension is written as:

$$\begin{aligned}\dot{\varepsilon} &= \dot{\varepsilon}_p + \dot{\varepsilon}_e \\ &= \dot{\varepsilon}_p + \frac{\dot{\sigma}}{E}\end{aligned} \tag{A11}$$

where $\dot{\sigma}$ is the macroscopic stress rate and E is the macroscopic elastic modulus of copper. Now we treat the strain rates as functions of J that $\dot{\varepsilon}(J) = \dot{\varepsilon}_p(J) + \dot{\varepsilon}_e(J)$. By applying a sudden change of current density and imposing the loading boundary condition: $\dot{\varepsilon}(0) = \dot{\varepsilon}(J) = 5\times10^{-3}\text{s}^{-1}$, we get:

$$\dot{\varepsilon}_p(0) + \frac{\dot{\sigma}(0)}{E} = \dot{\varepsilon}_p(J) + \frac{\dot{\sigma}(J)}{E} \tag{A12}$$

Thus,

$$\dot{\varepsilon}_p(0) = \dot{\varepsilon}_p(J) + \frac{\dot{\sigma}(J)}{E} - \frac{\dot{\sigma}(0)}{E} = \dot{\varepsilon}_p(J) - \frac{1}{E}\left[\dot{\Delta\sigma}(J)\right] \tag{A13}$$

where $\Delta\sigma(J) \triangleq \sigma(0) - \sigma(J)$. As $\dot{\Delta\sigma}(J) = \frac{d\Delta\sigma(J)}{d\varepsilon}\frac{d\varepsilon}{dt} = \frac{d\Delta\sigma(J)}{d\varepsilon}\dot{\varepsilon}$, we then could derive:

$$\dot{\varepsilon}_p(0) = \dot{\varepsilon}_p(J) - \frac{1}{E}\frac{d\Delta\sigma(J)}{d\varepsilon}\dot{\varepsilon} \tag{A14}$$

Here, the values measured at $\varepsilon_1 = 0.11$ and $\varepsilon_2 = 0.25$ under J = 100A/mm^2 are applied for estimation the magnitude of $\frac{1}{E}\frac{d\Delta\sigma(J)}{d\varepsilon}$. We have subsequently:

$$\frac{1}{E}\frac{d\Delta\sigma(J)}{d\varepsilon} \sim \frac{1}{E}\frac{\Delta\sigma(J,\varepsilon_2) - \Delta\sigma(J,\varepsilon_1)}{\varepsilon_2 - \varepsilon_1} = \frac{1}{120\text{GPa}}\frac{0.1\text{MPa}}{0.14} \sim 10^{-5} \tag{A15}$$

This magnitude is extremely small, so, we get that:

$$\begin{aligned}\dot{\varepsilon}_p(0) &= \dot{\varepsilon}_p(J) - 10^{-5}\cdot\dot{\varepsilon}(0) \\ &= \dot{\varepsilon}_p(J) - 10^{-5}\cdot\left(\dot{\varepsilon}_p(0) + \dot{\varepsilon}_e(0)\right) \\ \Rightarrow \dot{\varepsilon}_p(J) &= \dot{\varepsilon}_p(0) + 10^{-5}\cdot\left(\dot{\varepsilon}_p(0) + \dot{\varepsilon}_e(0)\right)\end{aligned} \tag{A16}$$

Conventionally, $\dot{\varepsilon}_e$ is smaller than $\dot{\varepsilon}_p$ at the plastic deformation stage. By approximation, the assumption adopted in Section 4.4 is verified. The imposed loading boundary condition gives directly:

$$\dot{\varepsilon}_p(0) = \dot{\varepsilon}_p(J) \tag{A17}$$

Appendix 4. Measurement resolution Analysis

To validate the sufficiency of the real resolution, we employed two independent (see Fig. A1) analysis on the machine noise. The first involved a stress relaxation test (Fig. A1(a)), in which a sample is loaded with the same strain rate ($0.005s^{-1}$) to 400N. Then the strain was maintained. The 2σ of the baseline noise over a 1500 ms window was determined to be 0.031 MPa. The second method utilized the linearity of the work-hardening region (Fig. A1 (b)) on the current-free stress-strain data. By performing a linear fit (strain range: 17.4%–17.9%) and calculating the residual standard deviation (RSD), we obtained a 2 × RSD of 0.035 MPa. These results consistently indicate a resolution on the order of ±0.03 MPa.

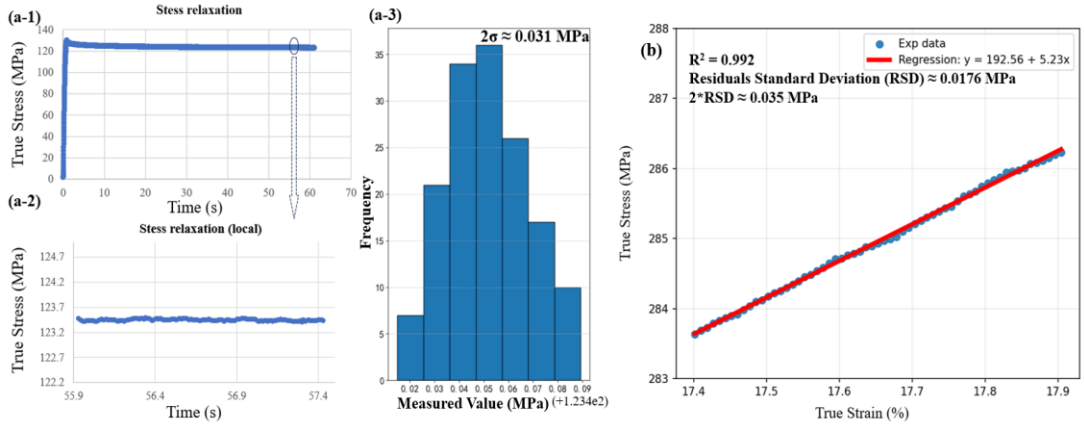

Fig A1. System resolution analysis. (a-1) System noise analysis by stress-relaxation test. (a-2) Magnified stress plateau. (a-3) Statistics of the measured value of the plateau, showing great normal distribution with 2σ = 0.031MPa. (b) Noise analysis on a segment of the stress-strain curve.

Appendix 5. Additional validation of the model

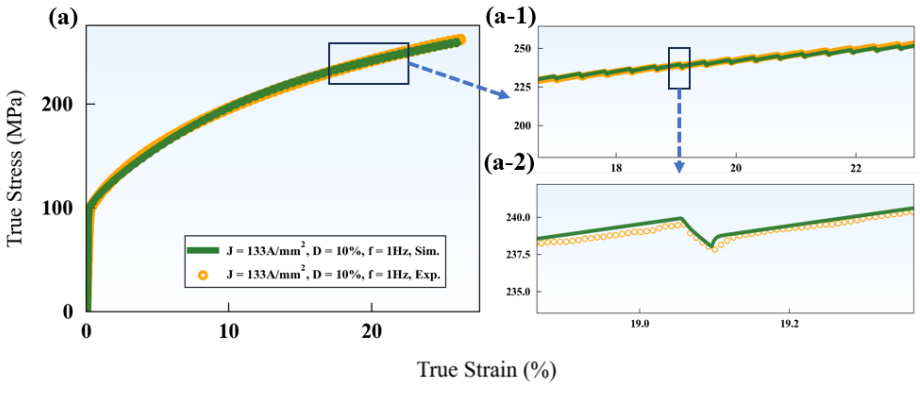

Fig A2. A validation case to further prove the validity of the model. (a) Macroscopic strain-stress comparison. (a-1) and (a-2) Magnified views of the macroscopic strain-stress comparison, showing detailed stress responses accurately captured by the EC-EVPSC model.

CRediT authorship contribution statement:

Kaiwei Wu: Conceptualization, Data Curation, Formal analysis, Investigation, Methodology, Project Management, Visualization, Writing-original draft, Writing-review & editing. **Xiaochuan Sun:** Software, Formal analysis, Investigation, Methodology, Project Management, Supervision, Writing-review & editing. **Bowen Liu:** Data Curation, Investigation, Methodology, Validation. **Quan Li:** Methodology, Writing-review & editing. **Wei Wen:** Investigation, Writing-review & editing. **Qiwei Shi:** Data Curation, Funding Acquisition, Methodology, Resources, Software, Supervision, Writing-review & editing. **Zhutian Xu:** Resources. **Linfa Peng:** Resources. **Huamiao Wang:** Conceptualization, Supervision, Writing-review & editing. **Yin Zhang:** Validation, Writing - review & editing. **Samuel Forest:** Investigation, Supervision, Validation, Writing - review & editing.

Declaration of competing interest:

The authors declare that they have no known competing financial interests or personal relationships that could have appeared to influence the work reported in this paper.

Acknowledgments:

The authors would like to gratefully acknowledge the support of the National Natural Science Foundation of China (Grant No. 52273229). This work is also financially supported by the MAI (Materials Ageing Institute, http://themai.org) of France. In addition, the authors would like to gratefully acknowledge State Key Laboratory of Mechanical System and Vibration of Shanghai Jiao Tong University for supports on the experimental electricity source and the EAD platform.

Data availability:

Data will be available on request.

Reference:

Agnew, S.R., Mehrotra, P., Lillo, T.M., Stoica, G.M., Liaw, P.K., 2005. Texture evolution of five wrought magnesium alloys during route A equal channel angular extrusion: Experiments and simulations. Acta Materialia 53, 3135-3146.

Akhondzadeh, S., Sills, R.B., Bertin, N., Cai, W., 2020. Dislocation density-based plasticity model from massive discrete dislocation dynamics database. Journal of the Mechanics and Physics of Solids 145, 104152.

Aksenova, K., Zaguliaev, D., Konovalov, S., Shlyarov, V., Ivanov, Y., 2022. Influence of Constant Magnetic Field upon Fatigue Life of Commercially Pure Titanium. Materials (Basel) 15.

Alshits, V.I., Darinskaya, E.V., Kazakova, O.L., Mikhina, E.Y., Petrzhik, E.A., 1997. Magnetoplastic effect in nonmagnetic crystals. Materials Science and Engineering: A 234-236, 617-620.

Anderson, P.M., Hirth, J.P., Lothe, J., 2017. Theory of dislocations. Cambridge University Press.

Ao, D., Chu, X., Yang, Y., Lin, S., Gao, J., 2018. Effect of electropulsing on springback during V-bending of Ti-6Al-4V titanium alloy sheet. The International Journal of Advanced Manufacturing Technology 96, 3197-3207.

Arsenlis, A., Parks, D., 1999. Crystallographic aspects of geometrically-necessary and statistically-stored dislocation density. Acta materialia 47, 1597-1611.

Austin, R.A., McDowell, D.L., 2011. A dislocation-based constitutive model for viscoplastic deformation of fcc metals at very high strain rates. International Journal of Plasticity 27, 1-24.

Bardeen, J., Cooper, L.N., Schrieffer, J.R., 1957a. Microscopic theory of superconductivity. Physical Review 106, 162.

Bardeen, J., Cooper, L.N., Schrieffer, J.R., 1957b. Theory of superconductivity. Physical review 108, 1175.

Bassani, J.L., Wu, T.-Y., 1991. Latent hardening in single crystals. II. Analytical characterization and predictions. Proceedings of the Royal Society of London. Series A: Mathematical and Physical Sciences 435, 21-41.

Beyerlein, I.J., Tomé, C.N., 2008. A dislocation-based constitutive law for pure Zr including temperature effects. International Journal of Plasticity 24, 867-895.

Bilyk, S.R., Ramesh, K.T., Wright, T.W., 2005. Finite deformations of metal cylinders subjected to electromagnetic fields and mechanical forces. Journal of the Mechanics and Physics of Solids 53, 525-544.

Bong, H.J., Lee, J., Lee, M.-G., Kim, D., 2019. Identification of mechanical responses of steel sheets under non-proportional loadings using dislocation-density based crystal plasticity model. International Journal of Mechanical Sciences 155, 461-474.

Borbély, A., 2022. The modified Williamson-Hall plot and dislocation density evaluation from diffraction peaks. Scripta Materialia 217, 114768.

Čebron, M., Kosel, F., 2014. Stored energy predictions from dislocation-based hardening models and hardness measurements for tensile-deformed commercial purity copper. Strojniški vestnik-Journal of Mechanical Engineering 60, 462-474.

Cheong, K.S., Busso, E.P., Arsenlis, A., 2005. A study of microstructural length scale effects on the behaviour of FCC polycrystals using strain gradient concepts. International Journal of Plasticity 21, 1797-1814.

Chuan, W., Wei, L.H., Lu, L., Yuan, W.Y., 2024. Electrical-thermal-mechanical coupled modeling and simulation on deformation behaviors of Ti6554 alloy in electrically-assisted micro-tension. Computational Materials Science 231, 112567.

Cuitino, A.M., Ortiz, M., 1993. Computational modelling of single crystals. Modelling and Simulation in Materials Science and Engineering 1, 225.

Dai, Z., Jin, K., Kou, Y., 2024. An electroplastic constitutive model of fcc metals and their alloys under high current density. Mechanics of Materials 189, 104878.

Dimitrov, N.K., Liu, Y., Horstemeyer, M.F., 2021. Experimental Observation and Modelling of the Electroplastic Effect in Nonferromagnetic Ductile Metals. Experimental Techniques 45, 735-748.
Franciosi, P., Berveiller, M., Zaoui, A., 1980. Latent hardening in copper and aluminium single crystals. Acta Metallurgica 28, 273-283.
Freudenberger, J., Warlimont, H., 2018. Copper and copper alloys, Springer Handbook of Materials Data. Springer, pp. 297-305.
Gao, H., Huang, Y., 2003. Geometrically necessary dislocation and size-dependent plasticity. Scripta Materialia 48, 113-118.
Gao, J., Li, H., Sun, X., Zhang, X., Zhan, M., 2022. Electro-thermal-mechanical coupled crystal plasticity modeling of Ni-based superalloy during electrically assisted deformation. International Journal of Plasticity 157, 103397.
Gérard, C., Cailletaud, G., Bacroix, B., 2013. Modeling of latent hardening produced by complex loading paths in FCC alloys. International journal of plasticity 42, 194-212.
Ghassemali, E., Tan, M.-J., Wah, C.B., Lim, S.C.V., Jarfors, A.E.W., 2015. Effect of cold-work on the Hall–Petch breakdown in copper based micro-components. Mechanics of Materials 80, 124-135.
Gouriet, K., Hilairet, N., Amiguet, E., Bolfan-Casanova, N., Wang, Y., Reynard, B., Cordier, P., 2015. Plasticity of the dense hydrous magnesium silicate phase A at subduction zones conditions. Physics of the Earth and Planetary Interiors 248, 1-11.
Guo, Y., Lee, Y.J., Zhang, Y., Wang, H., 2022. Magneto-plasticity in micro-cutting of single-crystal copper. Journal of Materials Science & Technology 124, 121-134.
Hall, E., 1951. The deformation and ageing of mild steel: III discussion of results. Proceedings of the Physical Society. Section B 64, 747.
Hayt Jr, W., 1989. Engineering electromagnetics 5th edition. New York, McGraw-Hill international edition.
He, J., Zeng, Z., Li, H., Wang, S., 2020. The microstructure and mechanical properties of copper in electrically assisted tension. Materials & Design 196, 109171.
Hull, D., Bacon, D.J., 2011. Introduction to dislocations. Elsevier.
Jemielniak, R., Krolikowski, J., 1985. Ultrasonic attenuation from dislocations in a magnetic field. Le Journal de Physique Colloques 46, C10-163-C110-166.
Jiang, J., Britton, T., Wilkinson, A., 2013. Evolution of dislocation density distributions in copper during tensile deformation. Acta Materialia 61, 7227-7239.
Jiang, J., Britton, T.B., Wilkinson, A.J., 2015. The orientation and strain dependence of dislocation structure evolution in monotonically deformed polycrystalline copper. International Journal of Plasticity 69, 102-117.
Jones, J.J., Mears, L., 2011. Constant Current Density Compression Behavior of 304 Stainless Steel and Ti-6Al-4V During Electrically-Assisted Forming, ASME 2011 International Manufacturing Science and Engineering Conference, pp. 629-637.
Jones, J.J., Mears, L., Roth, J.T., 2012. Electrically-Assisted Forming of Magnesium AZ31: Effect of Current Magnitude and Deformation Rate on Forgeability. Journal of Manufacturing Science and Engineering 134.
Kang, J., Liu, X., Niezgoda, S.R., 2022. Crystal plasticity modeling of ultrasonic softening

effect considering anisotropy in the softening of slip systems. International Journal of Plasticity 156, 103343.
Kim, M.-J., Lee, M.-G., Hariharan, K., Hong, S.-T., Choi, I.-S., Kim, D., Oh, K.H., Han, H.N., 2017. Electric current–assisted deformation behavior of Al-Mg-Si alloy under uniaxial tension. International Journal of Plasticity 94, 148-170.
Kinsey, B., Cullen, G., Jordan, A., Mates, S., 2013. Investigation of electroplastic effect at high deformation rates for 304SS and Ti–6Al–4V. CIRP Annals 62, 279-282.
Kittel, C., McEuen, P., 2018. Introduction to solid state physics. John Wiley & Sons.
Kocks, U., 1966. A statistical theory of flow stress and work-hardening. Philosophical Magazine 13, 541-566.
Kocks, U.F., Argon, A.S., Ashby, M.F., 1975. Thermodynamics and Kinetics of Slip. Pergamon Press.
Konijnenberg, P.J., Zaefferer, S., Raabe, D., 2015. Assessment of geometrically necessary dislocation levels derived by 3D EBSD. Acta Materialia 99, 402-414.
Lahiri, A., Shanthraj, P., Roters, F., 2019. Understanding the mechanisms of electroplasticity from a crystal plasticity perspective. Modelling and Simulation in Materials Science and Engineering 27, 085006.
Lebensohn, R.A., Tomé, C.N., 1993. A self-consistent anisotropic approach for the simulation of plastic deformation and texture development of polycrystals: Application to zirconium alloys. Acta Metallurgica et Materialia 41, 2611-2624.
Lee, T., Magargee, J., Ng, M.K., Cao, J., 2017. Constitutive analysis of electrically-assisted tensile deformation of CP-Ti based on non-uniform thermal expansion, plastic softening and dynamic strain aging. International Journal of Plasticity 94, 44-56.
Lei, M., Huang, J., Li, Y., Zhang, L., Yang, G., Wen, B., 2025. High-strain-rate mechanical constitutive modeling with computational parameters. International Journal of Plasticity 189, 104329.
Li, C., Xu, Z., Peng, L., Lai, X., 2022a. An electric-pulse-assisted stamping process towards springback suppression and precision fabrication of micro channels. International Journal of Mechanical Sciences 218, 107081.
Li, D., Yu, E., Liu, Z., 2013. Microscopic mechanism and numerical calculation of electroplastic effect on metal's flow stress. Materials Science and Engineering: A 580, 410-413.
Li, W., Shen, Y., Liu, H., Wang, Y., Zhu, W., Xie, C., 2016. Non-octahedral-like dislocation glides in aluminum induced by athermal effect of electric pulse. Journal of Materials Research 31, 1193-1200.
Li, X., Turner, J., Bustillo, K., Minor, A.M., 2022b. In situ transmission electron microscopy investigation of electroplasticity in single crystal nickel. Acta Materialia 223, 117461.
Li, X., Zhu, Q., Hong, Y., Zheng, H., Wang, J., Wang, J., Zhang, Z., 2022c. Revealing the pulse-induced electroplasticity by decoupling electron wind force. Nature Communications 13, 6503.
Liang, C.-L., Lee, S.-W., Lin, K.-L., 2017. The mechanism of an increase in electrical resistance in Al thin film induced by current stressing. Thin Solid Films 636, 164-170.
Liang, H., Dunne, F.P.E., 2009. GND accumulation in bi-crystal deformation: Crystal

plasticity analysis and comparison with experiments. International Journal of Mechanical Sciences 51, 326-333.
Liu, Y., Meng, B., Du, M., Wan, M., 2022. Electroplastic effect and microstructural mechanism in electrically assisted deformation of nickel-based superalloys. Materials Science and Engineering: A 840, 142975.
Lu, L., Shen, Y., Chen, X., Qian, L., Lu, K., 2004. Ultrahigh Strength and High Electrical Conductivity in Copper. Science 304, 422-426.
Madec, R., Devincre, B., Kubin, L.P., 2002. From dislocation junctions to forest hardening. Physical review letters 89, 255508.
Meissner, W., Ochsenfeld, R., 1933. Ein neuer effekt bei eintritt der supraleitfähigkeit. Naturwissenschaften 21, 787-788.
Molotskii, M., Fleurov, V., 1995. Magnetic effects in electroplasticity of metals. Physical review B 52, 15829.
Molotskii, M., Fleurov, V., 1997a. Manifestations of hyperfine interaction in plasticity. Physical Review B 56, 10809-10811.
Molotskii, M., Fleurov, V., 1997b. Spin Effects in Plasticity. Physical Review Letters 78, 2779-2782.
Molotskii, M.I., 2000. Theoretical basis for electro- and magnetoplasticity. Materials Science and Engineering: A 287, 248-258.
Molotskii, M.I., Kris, R.E., Fleurov, V., 1995. Internal friction of dislocations in a magnetic field. Physical Review B 51, 12531-12536.
Nemat-Nassar, S., Asaro, R.J., Hegemier, G.A., 2012. Theoretical foundation for large-scale computations for nonlinear material behavior. Springer Science & Business Media.
Niu, H.T., Gao, P.F., Li, H.W., Zhan, M., 2025. Mechanism and modelling of the electroplastic effect in titanium alloy: From the perspective of dislocation slip. International Journal of Plasticity 192, 104405.
Orowan, E., 1940. Problems of plastic gliding. Proceedings of the Physical Society 52, 8.
Petch, N.J., 1953. The cleavage strength of polycrystals. J. Iron Steel Inst. 174, 25-28.
Ren, X., Wang, Z., 2025. Electron-dislocation interactions in electroplastic effects of pure aluminum: Thermal fluctuation-assisted electron wind mechanism. Computational Materials Science 253, 113818.
Rudolf, C., Goswami, R., Kang, W., Thomas, J., 2021. Effects of electric current on the plastic deformation behavior of pure copper, iron, and titanium. Acta Materialia 209, 116776.
Ruszkiewicz, B.J., Grimm, T., Ragai, I., Mears, L., Roth, J.T., 2017. A review of electrically-assisted manufacturing with emphasis on modeling and understanding of the electroplastic effect. Journal of Manufacturing Science and Engineering 139, 110801.
Saada, G., 1995. Dynamical effects in crystal plasticity. Key Engineering Materials 97, 275-286.
Savitzky, A., Golay, M.J., 1964. Smoothing and differentiation of data by simplified least squares procedures. Analytical chemistry 36, 1627-1639.
Silveira, V., Porto, M., Mannheimer, W., 1981. Electroplastic effect in copper subjected to low density electric current. Scripta Metallurgica 15, 945-950.
Siopis, M.S., Kinsey, B.L., Kota, N., Ozdoganlar, O.B., 2011. Effect of Severe Prior

Deformation on Electrical-Assisted Compression of Copper Specimens. Journal of Manufacturing Science and Engineering 133.
Sprecher, A., Mannan, S., Conrad, H., 1986. Overview no. 49: On the mechanisms for the electroplastic effect in metals. Acta Metallurgica 34, 1145-1162.
Stangebye, S., Zhang, Y., Gupta, S., Zhu, T., Pierron, O., Kacher, J., 2022. Understanding and quantifying electron beam effects during in situ TEM nanomechanical tensile testing on metal thin films. Acta Materialia 222, 117441.
Stricker, M., Weygand, D., 2015. Dislocation multiplication mechanisms–Glissile junctions and their role on the plastic deformation at the microscale. Acta Materialia 99, 130-139.
Sun, X., Zhou, K., Liu, C., Zhang, X., Wang, H., Wang, G., Peng, L., 2024. A crystal plasticity based strain rate dependent model across an ultra-wide range. International Journal of Plasticity 180, 104056.
Sutton, A., Todorov, T., 2021. Theory of electroplasticity based on electromagnetic induction. Physical review materials 5, 113605.
Takeuchi, N., Iizuka, M., Kemmotsu, K., Ando, D., Ishida, K., Sutou, Y., 2025. Realization of high resistivity and low-temperature coefficient of resistivity in Fe-20Mn-11Al-5Cr-1C-0.01B alloy through microstructure control. Materials Characterization 229, 115499.
Tang, G., Zhang, J., Zheng, M., Zhang, J., Fang, W., Li, Q., 2000. Experimental study of electroplastic effect on stainless steel wire 304L. Materials Science and Engineering: A 281, 263-267.
Taylor, G.I., 1934. The mechanism of plastic deformation of crystals. Part I.—Theoretical. Proceedings of the Royal Society of London. Series A, Containing Papers of a Mathematical and Physical Character 145, 362-387.
Tiwari, J., Balaji, V., Krishnaswamy, H., Amirthalingam, M., 2022. Dislocation density based modelling of electrically assisted deformation process by finite element approach. International Journal of Mechanical Sciences 227, 107433.
Wang, H., Capolungo, L., Clausen, B., Tomé, C.N., 2017. A crystal plasticity model based on transition state theory. International Journal of Plasticity 93, 251-268.
Wang, H., Clausen, B., Capolungo, L., Beyerlein, I.J., Wang, J., Tomé, C.N., 2016. Stress and strain relaxation in magnesium AZ31 rolled plate: In-situ neutron measurement and elastic viscoplastic polycrystal modeling. International Journal of Plasticity 79, 275-292.
Wang, H., Wu, P.D., Tomé, C.N., Huang, Y., 2010. A finite strain elastic–viscoplastic self-consistent model for polycrystalline materials. Journal of the Mechanics and Physics of Solids 58, 594-612.
Wang, R., Lu, C., Tieu, K.A., Gazder, A.A., 2022. Slip system activity and lattice rotation in polycrystalline copper during uniaxial tension. Journal of Materials Research and Technology 18, 508-519.
Wang, S., Hashimoto, N., Wang, Y., Ohnuki, S., 2013. Activation volume and density of mobile dislocations in hydrogen-charged iron. Acta materialia 61, 4734-4742.
Wu, T.-Y., Bassani, J.L., Laird, C., 1991. Latent hardening in single crystals-I. Theory and experiments. Proceedings of the Royal Society of London. Series A: Mathematical and Physical Sciences 435, 1-19.
Xiang, S., Zhang, X., 2019. Dislocation structure evolution under electroplastic effect.

Materials Science and Engineering: A 761, 138026.
Xu, Z., Jiang, T., Huang, J., Peng, L., Lai, X., Fu, M.W., 2022. Electroplasticity in electrically-assisted forming: Process phenomena, performances and modelling. International Journal of Machine Tools and Manufacture 175, 103871.
Xu, Z., Li, X.n., Zhang, R., Ma, J., Qiu, D., Peng, L., 2023. The effect of electric current on dislocation activity in pure aluminum: A 3D discrete dislocation dynamics study. International Journal of Plasticity 171, 103826.
Yan, J., Zhao, R., Wan, M., Meng, B., 2023. Coupled effect of pulsed current and ultrasonic vibration on deformation behavior of Inconel 718 sheet: phenomena and modeling. Journal of Materials Research and Technology 25, 5538-5560.
Yang, Y., Qin, R., Dong, Y., Wang, J., Ye, C., 2023a. Crystal plasticity modeling of electropulsing induced plasticity in metals. International Journal of Plasticity 171, 103828.
Yang, Y., Wang, Y., Lu, H., Wang, Z., Xie, D., Zhao, Y., Du, J., Wang, C., Ma, E., Shan, Z., 2023b. Significant mechanical softening of copper under coupled electric and magnetic stimuli. Scripta materialia 231, 115438.
Zecevic, M., Beyerlein, I.J., Knezevic, M., 2018. Activity of pyramidal I and II< c+ a> slip in Mg alloys as revealed by texture development. Journal of the Mechanics and Physics of Solids 111, 290-307.
Zehetbauer, M., Seumer, V., 1993. Cold work hardening in stages IV and V of FCC metals—I. Experiments and interpretation. Acta metallurgica et materialia 41, 577-588.
Zhang, S., Lu, Y., Gong, X., Shen, Z., 2018. Investigation of Current Parameters and Size Effects on Mechanical Properties During Pulsed Electrically Assisted Uniaxial Tension in T2 Red Copper Sheets. Journal of Materials Engineering and Performance 27, 6493-6504.
Zhang, X., Li, H., Zhan, M., Zheng, Z., Gao, J., Shao, G., 2020. Electron force-induced dislocations annihilation and regeneration of a superalloy through electrical in-situ transmission electron microscopy observations. Journal of Materials Science & Technology 36, 79-83.
Zhao, J., Ren, Z., Zhang, H., Wang, G.-X., Dong, Y., Ye, C., 2019. Electroplasticity in AZ31B subjected to short-duration high-frequency pulsed current. Journal of Applied Physics 125.
Zhao, S., Zhang, R., Chong, Y., Li, X., Abu-Odeh, A., Rothchild, E., Chrzan, D.C., Asta, M., Morris, J.W., Minor, A.M., 2021. Defect reconfiguration in a Ti–Al alloy via electroplasticity. Nature Materials 20, 468-472.
Zheng, X., Yi, M., 2025. An Electro-thermo-mechanically Coupled Crystal Plasticity Model for Electroplasticity. Acta Mechanica Solida Sinica.
Zhong, H., Shi, Q., Dan, C., You, X., Zong, S., Zhong, S., Zhang, Y., Wang, H., Chen, Z., 2024. Resolving localized geometrically necessary dislocation densities in Al-Mg polycrystal via in situ EBSD. Acta Materialia 279, 120290.
Zhu, G., Wang, L., Sun, Y., Shang, X., Wang, J., Wang, H., Zeng, X., 2021. Grain-size effect on the deformation of Mg–3Al–3Sn alloy: Experiments and elastic-viscoplastic self-consistent modeling. International Journal of Plasticity 143, 103018.